High-fidelity Aerostructural Optimization of Tow-steered Composite Wings

Timothy R. Brooks[*], Joaquim R. R. A. Martins

University of Michigan, Department of Aerospace Engineering, Ann Arbor, Michigan, United States

Graeme J. Kennedy

Georgia Institute of Technology, School of Aerospace Engineering, Atlanta, Georgia, United States

---

Abstract

Over the past several decades, composites have increasingly become the material of choice in modern aircraft structural design. This is primarily due to the high stiffness- and strength-to-weight ratios offered by conventional composites when compared to metals. Unconventional composite designs, such as tow-steered composites, have demonstrated potential for further expanding these advantages. Unlike their conventional composite counterparts, tow-steered composites feature layers with spatially varying fiber orientations. When applied to wing design, tow-steered composites offer an increase in design freedom at the cost of higher design complexity, making them ideal candidates for design optimization. We develop a methodology for the aerostructural design optimization of tow-steered composite wings using high-fidelity physics models. We also quantify the benefits of this new technology by performing a fuel burn minimization for both a tow-steered and a conventional composite wing design. This assessment is done for the undeflected Common Research Model, which is representative of a twin-aisle transport aircraft. We find improvements of up to 2.4% in fuel burn and 24% in wing weight relative to the optimized conventional composite design. We show that this improvement is due to a combination of improved passive aeroelastic tailoring and local strength tailoring in high-stress regions in the tow-steered structure. For a higher-aspect-ratio (13.5) wing design, we find improvements of up to 1.5% and 14% in fuel savings and wing weight, respectively. To better understand the effect of aspect ratio on tow-steered wing design, we perform an optimization study where the aspect ratio is varied between 7.5 and 13.5. We found that there are diminishing returns in the benefit of tow steering as the aspect ratio is increased because less passive load alleviation is possible.

Keywords: Variable angle tow, optimization, tow steering, wing design, aeroelastic tailoring

---

Nomenclature

a_g	Gap tow add rule

---

[*] Corresponding author at: University of Michigan, Department of Aerospace Engineering, Ann Arbor, Michigan, United States.

Email address: `timryanb@umich.edu` (Timothy R. Brooks)

a_o	Overlap tow drop rule
$\boldsymbol{A}$	Laminate membrane stiffness matrix
d	Wingbox depth
$\boldsymbol{D}$	Laminate bending stiffness matrix
$D_{11}, D_{12}, D_{11}, D_{66}$	Laminate/skin bending stiffness matrix components
D_1, D_3, D_2	Smeared panel bending stiffness matrix components
EI_s	Effective panel bending stiffness
$E_1, E_2, G_{12}, G_{23}, G_{13}$	Ply stiffness moduli
$L_{\text{add}}, L_{\text{cut}}$	Minimum tow add and add lengths
L_x	Wingbox panel length
M_1, M_{12}, M_2	Laminate moment resultants
N_1, N_{12}, N_2	Laminate force resultants
R_{min}	Minimum tow-path turning radius
s_p	Stiffener pitch
t^{cp}	Panel thickness control point variables
t_p	Panel thickness
$\|\|\nabla t_0\|\|$	Minimum panel thickness gradient
$\vec{v}$	Tow-path tangent vector
X_t, X_c	Tensile and compressive ply strengths in fiber direction
Y_t, Y_c	Tensile and compressive ply strengths in transverse direction
S	Ply shear strength
θ_0	Main tow angle
κ	Tow-path curl
$\kappa_{xx}, \kappa_{xy}, \kappa_{yy}$	Laminate bending curvatures
ν_{12}	Ply in-plane Poisson's ratio
ψ	Tow-path divergence
ψ_1	Bend-twist coupling parameter

1. Introduction

The automated fiber placing (AFP) machine has revolutionized the manufacturing of carbon-fiber-reinforced composite structures in general, and the manufacturing of aerostructures in particular [1, 2, 3]. AFP machines have robotic arms that lay down composites in a series of pre-impregnated, fiber-reinforced tows. When tow paths are programmed to be straight and alternate in orientation from layer to layer (e.g., 0°, ±45°, 90°), a conventional composite laminate can be efficiently produced. This has led to a rapid growth in the use of composites as a "black metal" replacement for metallic structures in the aerospace industry, making it possible to design lighter, more efficient structures.

There is no requirement that the tow paths in the composite layup must be straight. When curved tow paths are specified in each layer, the resulting composite is referred to as *tow-steered*. Since the directional stiffness and strength of a composite are inherently dependent on the local fiber direction in each layer, tow steering offers a significant increase in design freedom over conventional composites. For simple laminate designs, researchers have already demonstrated that tow-steered panels can be designed to outperform their conventional counterparts in terms of maximum strength [4, 5, 6] and buckling performance [7, 8, 9]. A number of researchers have demonstrated that these benefits are not just theoretical; they are realizable through the manufacturing of tailored, tow-steered structures [10, 11, 12, 13].

Despite these benefits, tow-steered composites have yet to be utilized in a major aircraft structural component. Given that recent transport aircraft, such as the Airbus A350XWB and the Boeing 787, contain as much as 50% composite materials by structural weight [14] [1], it is surprising that aircraft manufacturers have yet to take full advantage of the benefits offered by tow-steered composites. One reason for this is the difficulty in defining certification standards for these unconventional laminates. The second reason is that there is only limited work quantifying the benefits of adding tow steering into the composite design of complex structural components, such as the wing structure. Another challenge in the design of tow-steered structures is that it is not obvious nor intuitive what the tow paths should be for such a structure so that it maximizes the benefits offered by its variable directional stiffness properties. The goal of the present work is to address the latter two difficulties by developing a methodology for performing high-fidelity multidisciplinary design optimization (MDO) of tow-steered structures, and quantifying the benefits of tow steering for flexible-wing design.

Some researchers have already started to use MDO to estimate the performance benefits of tow-steered composite wings. Stodieck et al. [15] investigated the benefits of tow-steered composites when applied to wing design. In their work, they minimized the structural wing weight of the Common Research Model (CRM) aircraft considering several structural sizing maneuver flight conditions and found that by adding tow steering to the design, they could reduce the wing structural weight by up to 12% relative to a conventional unsteered design. This study also included consideration for dynamic flight conditions (gust analysis and flutter onset), but these constraints were found to be largely inactive for the optimum design. Instead, the active constraints were mostly related to static maneuver flight conditions.

A similar study by Stanford and Jutte [16] investigated high-aspect-ratio wing design and found up to an 8.8% reduction in structural weight. The structural weight reductions in these studies were made possible through a combination of additional structural and aeroelastic tailoring of the wing structure enabled by tow-steered composites.

The work presented here differs from the previous studies mentioned above in several ways. First, we include wing twist and cross-sectional shape design variables, enabling the full aerodynamic shape optimization and aerostructural design trades. Second, while previous efforts used a medium-fidelity vortex-lattice method approach corrected with computational fluid dynamics (CFD) data to model the aerodynamics, the work presented herein uses a higher-fidelity aerodynamic model based on Reynolds-averaged Navier–Stokes (RANS) CFD. Lastly, we also consider the effect that wing aspect ratio has on the benefits offered by tow steering.

We solve a series of fuel burn optimization problems for an aircraft geometry based on the CRM. To quantify the benefits of tow steering, we perform the optimizations with both tow-steered and fixed-ply-orientation conventional composites. These design cases provide insight into the potential benefits of tow steering when applied to modern aircraft wing designs. We then compare the benefits of the same tow-steered optimized design with a second conventional composite design where the layup of the wing skins are free to be rotated by the optimizer. This is to quantify how much of the benefit on the tow-steered design is due to aeroelastic tailoring as opposed to the structural tailoring of load paths. We also perform the tow-steered and fixed-ply-orientation conventional composite design optimizations for a higher-aspect-ratio variant of the CRM that is more flexible. This provides insight into the benefits of tow steering for next-generation high-aspect-ratio wings. Finally, the effect of aspect ratio on the wing design performance is evaluated by re-optimizing the tow-steered and fixed-ply-orientation conventional composite designs for aspect ratios ranging from 7.5 to 13.5.

---

[1] `https://www.airbus.com/aircraft/passenger-aircraft/a350xwb-family/a350-1000.html`, Last accessed on January 20, 2019.

2. Computational Framework

The optimization methodology used in this study is based on the MACH (MDO for aircraft configurations with high fidelity) framework [17]. MACH is an optimization framework developed for high-fidelity aerostructural analysis and design optimization of aircraft wings that accounts for the wing flexibility in both performance evaluation and design. The framework's aerostructural solver is composed of a detailed computational structural mechanics (CSM) solver coupled to a CFD solver. The solver also features an efficient coupled adjoint approach for computing the design sensitivities with respect to large numbers of variables [17, 18]. The adjoint approach solves a linearization of the governing equations that yields accurate sensitivities. These sensitivities are then passed to a gradient-based optimizer, which is given the freedom to simultaneously optimize the aerodynamic shape and internal structural sizing of the aircraft wing. We provide a brief overview of the components of MACH in this below; for a more detailed description, please refer to our previous work [17, 19].

The aerodynamic solver used in MACH is ADFlow [20, 21], a second-order, finite-volume CFD solver. ADFlow has the capability to perform both Euler and RANS analysis on both structured multiblock and overset meshes. In this work, we use the RANS solver with the Spalart–Allmaras turbulence model. ADFlow is responsible for computing the aircraft aerodynamic loads and functions of interest—lift, drag, and moment—in the aerostructural solver. ADflow efficiently computes derivatives of its functions of interest through a discrete adjoint approach, which was implemented through the selective application of automatic differentiation [20, 22].

The structural solver in MACH is TACS (Toolkit for Analysis of Composite Structures) [23], which is an efficient parallel CSM solver that is particularly effective in the analysis of the thin-walled structures that are typical in airframes. TACS is responsible for computing the aircraft structural deformations and functions of interest—stress, buckling, and mass—in the aerostructural solver. Like its aerodynamic counterpart, TACS utilizes an adjoint approach for efficiently computing derivatives of its functions of interest with respect to the design variables [23].

The coupling procedure for the aerodynamic and structural solver involves interpolating the structural displacements from the surface of the CSM mesh to the surface of the CFD mesh and then extrapolating those displacements to the farfield of the CFD volume mesh. This mesh deformation is accomplished by the framework's mesh warping algorithm, which uses an inverse distance weighting mesh warping approach [24] to preserve the quality of the mesh, thus preserving the accuracy of the CFD model during deformation.

The aerostructural solution procedure in MACH is based on the aerodynamic and structural solvers and mesh warping algorithm. The procedure is a Gauss–Seidel approach, wherein the aerodynamic loads from the CFD model are passed as tractions to the CSM solver, which computes the elastic deformation of the structure [17]. These deformations are interpolated to the wing surface by tying each CFD surface node on the wing to its nearest CSM node with a series of rigid links [25, 26]. As mentioned previously, the mesh movement algorithm then propagates the deformations on the wing surface to the farfield of the CFD mesh. This results in new CFD mesh with a deflected wing profile, which is solved again to compute the updated aerodynamic loads. This procedure is then repeated until convergence. The aerostructural design derivatives are computed by coupling the adjoints of the aerodynamic and structural solvers. This allows us to compute design derivatives with respect to $O(10^3)$ design variables for little additional cost relative to the aerostructural Gauss–Seidel solution [17].

The aerostructural functions of interests and corresponding derivatives are provided by SNOPT (Sparse Nonlinear OPTimizer) [27], a quasi-Newton gradient-based optimizer. SNOPT then uses the provided information to iteratively solve the coupled design optimization problem. SNOPT is particularly efficient in the solution of optimization problems with a large number of sparse constraints, such as those that we consider in this work. The optimizer is connected to the aerostructural solver in Python through the pyOptSparse interface [28] [2].

3. Baseline Aircraft Model

The design optimizations problems considered in this work are performed on the undeflected Common Research Models (uCRM). These models are based on the aerodynamic benchmark NASA Common Research Model (CRM) developed by Vassberg et al. [29] and extended for use in aeroelastic design analysis and optimization by Brooks et al. [30]. The uCRM models developed by Brooks et al. [30] come in two variants. The first variant (uCRM-9) maintains the original wing planform of the CRM, with wing dimensions and structural topology similar to that of the Boeing 777 aircraft. The second variant (uCRM-13.5) features a modified wing design with a higher aspect ratio of 13.5, which is larger than any commercial transonic aircraft designs flying today. We perform optimizations on both models in this work to understand the effect of tow steering on both medium and high-aspect-ratio wing design.

Table 1: uCRM wing specifications.

Parameter	uCRM-9	uCRM-13.5
Aspect ratio	9.0	13.5
Span (m)	58.76	72.00
Reference area (m^2)	383.74	383.78
Quarter-chord sweep (deg)	35	35
MAC (m)	7.01	5.77

The planforms of each uCRM model are shown in Figure 1, and the design specifications are listed in Table 1. The geometry of both models include the aircraft wing, fuselage, and horizontal stabilizer. In these models, only the wing structure is modeled and considered to be flexible, while the remaining aircraft components are considered to be rigid. The wing structural model is composed of the upper and lower wing skins, ribs, and leading- and trailing-edge spars. The stiffeners of the design are included implicitly through a smeared stiffness approach, where their stiffness is added (“smeared”) into that of the ribs, skins, and spars [31]. This allows for the stiffeners’ design variables—height, width, and spacing—to be treated as continuous design variables by the optimizer. We model all wing structure components as composite laminates with the ply properties listed in Table 2.

For each uCRM model, we perform the CFD computation on an overset mesh with roughly 1.2 million volume cells. The engine nacelle, pylon, and vertical stabilizer are not considered. To

---

[2] `https://github.com/mdolab/pyoptsparse`

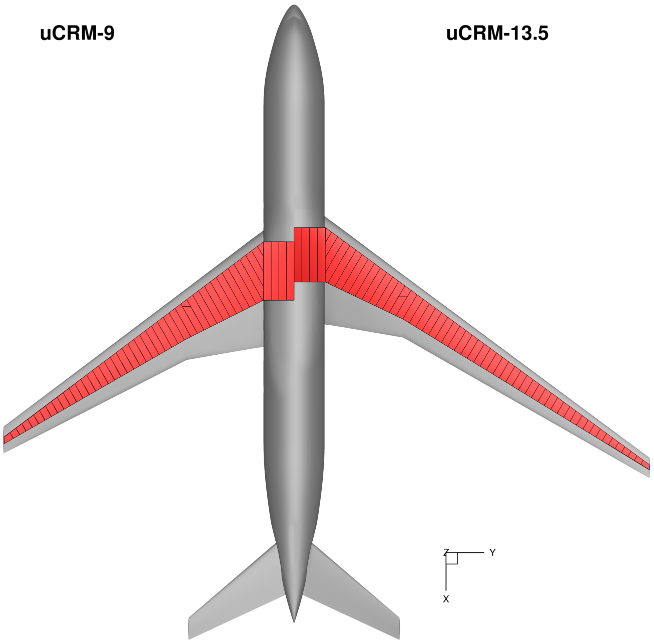

Figure 1: Wing and structural wingbox planform for the uCRM-9 (left) and uCRM-13.5 (right).

Table 2: Mechanical properties for the composites used on skin, ribs, and spars. X_t and X_c are the tensile and compressive ply strengths in the fiber direction, Y_t and Y_c are the respective strengths in the transverse direction, and S is the shear strength.

Material	E_1 [GPa]	E_2 [GPa]	G_{12} [GPa]	G_{13} [GPa]	G_{23} [GPa]	ν_{12}	X_t [MPa]	X_c [MPa]	Y_t [MPa]	Y_c [MPa]	S [MPa]	ρ [kg/m^3]
Unidirectional tape E752LT/AS4 (Skin)	117.9	9.7	4.8	4.8	4.8	0.34	1648	1034	64	228	71	1550
PW Fabric AS4/8552 (Ribs and Spars)	62.1	62.1	5	4.8	4.8	0.045	279	266	279	266	70	1550

account for the drag of these missing components, a fixed offset of 30 drag counts is added to the drag predicted by the CFD solver. The CSM mesh for each wing model has roughly 24,000 mixed interpolation tensorial component finite elements [32] with a total of about 136,000 degrees of freedom. An example of the CFD-CSM aerostructural solution at a 2.5 g maneuver condition for the uCRM-13.5 model is shown in Figure 2.

4. Structural Modeling

The procedure used to parameterize and model the conventional and tow-steered laminates considered in this work is based on the approach developed previously by the authors [33, 34]. In the remainder of this section, we provide an overview of this procedure. We only consider the skins of the wing structure to be steered, while the ribs and spars are modeled using conventional composite laminates. To avoid dependence on discrete design variables related to the laminate stacking sequence, for which a gradient-based optimizer is not well-suited, a smeared stiffness procedure is employed to model the laminate properties of the wingbox panels, similar to that used for the stiffeners.

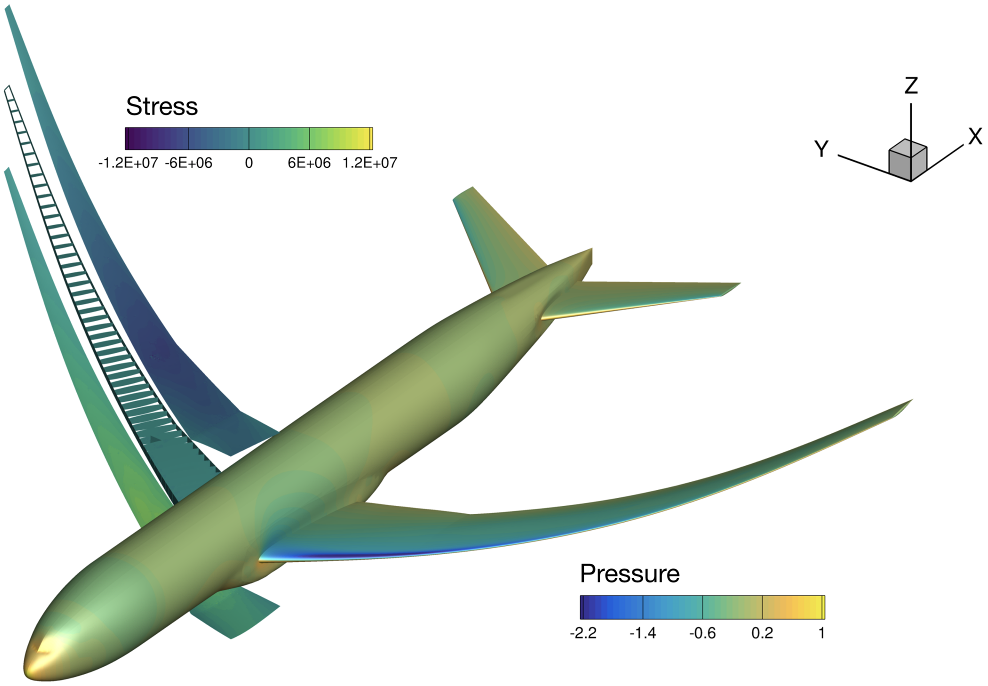

Figure 2: Aerostructural solution of the uCRM-13.5, showing the CSM stress distribution (left) and the CFD pressure distribution (right).

The first step in the structural modeling is to define the tow paths for each layer of the laminate. In theory, each layer of the laminate can take on a unique tow pattern. For relatively thick laminates with a large numbers of plies, like those used in wing structures, this requires a large number of design variables to parameterize. Since the number of iterations required to converge the optimization scales with the number of design parameters, this increase in design parameters may result in prohibitively expensive optimization problems. Therefore, we restrict each layer of the laminate to take on one of four unique tow patterns. This is done by first defining a reference tow orientation field, θ_0, using B-spline control points distributed over the laminate. This reference orientation field gives the local tow direction for the first tow pattern, referred to as the main tow pattern. The remaining three tow patterns are then defined by offsetting the main tow orientation by 45°, -45°, and 90°, such that the resulting laminate remains locally orthotropic with respect to the main tow path. If all tow orientation control point variables are set to zero, a conventional orthotropic laminate design (i.e., 0, ±45, 90°) can also be reproduced. The reference axis for all ply angles in the skins (i.e., the 0°-direction) is defined to be parallel to the leading edge of the wing.

An example of the tow pattern parameterization is shown in Figure 3. The percentage of the plies, or ply fractions, corresponding to each pattern is defined to remain constant throughout the laminate, and the main pattern makes up the majority of the plies and therefore contributes the most to the stiffness properties. Restricting the ply fractions to remain fixed during the optimization is not a limitation of the tow steering design process, but rather a simplifying assumption we make to isolate the structural and aeroelastic benefits offered by the actual steering of laminates

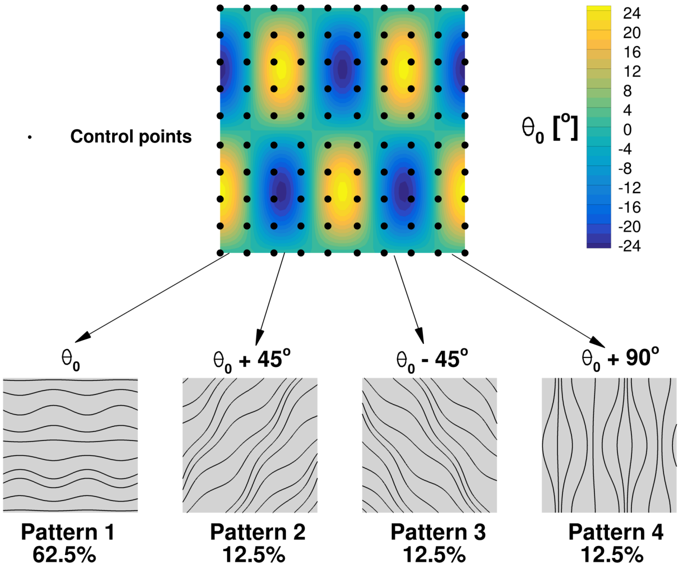

Figure 3: Example of the procedure used to define the main tow path and subsequent patterns.

from those due purely to the variation in ply fraction. This reduces the number of design variables necessary to parameterize the tow patterns of each ply down to one pattern. The ply fractions for each unique ply of each wingbox component are listed in Table 3.

Table 3: Ply fraction breakdown by wingbox component

Component	Patterns	Pattern ply fractions
Skins	$\{\theta_0 + 0°, \theta_0 + 45°, \theta_0 - 45°, \theta_0 + 90°\}$	$\{0.625, 0.125, 0.125, 0.125\}$
Spars	$\{0°, 45°, -45°, 90°\}$	$\{0.125, 0.375, 0.375, 0.125\}$
Ribs	$\{0°, 45°, -45°, 90°\}$	$\{0.375, 0.375, 0.125, 0.125\}$

In the second step of the modeling procedure, the stiffness properties of each pattern are smeared through the thickness of the laminate based on their respective ply fractions. This approximation works well for laminates with large numbers of plies with a uniform stacking sequence [35]. This allows us to neglect the dependence of laminate stiffness on stacking sequence and treat the local panel thickness as an independent continuous design variable. Finally, the panel thickness is assigned spatially using the same B-spline control points from the tow path definition step.

Typical conventional and tow-steered composite wingbox designs resulting from this parameterization are shown in Figure 4. The procedure for taking this information and converting it into the necessary layup instructions for the AFP machine is straightforward. The tow patterns specify to the AFP machine the local direction of tows for the plies of the laminate as a function of spatial location. The number of plies of each pattern to be laid by the AFP machine can be computed by multiplying the local panel thickness and ply fractions and rounding the value for each pattern to the nearest ply. We used this laminate design approach to design a tow-steered wing structure that was manufactured by Aurora Flight Sciences as a third sub-scale test article [13], demonstrating that the approach results in physically realizable designs.

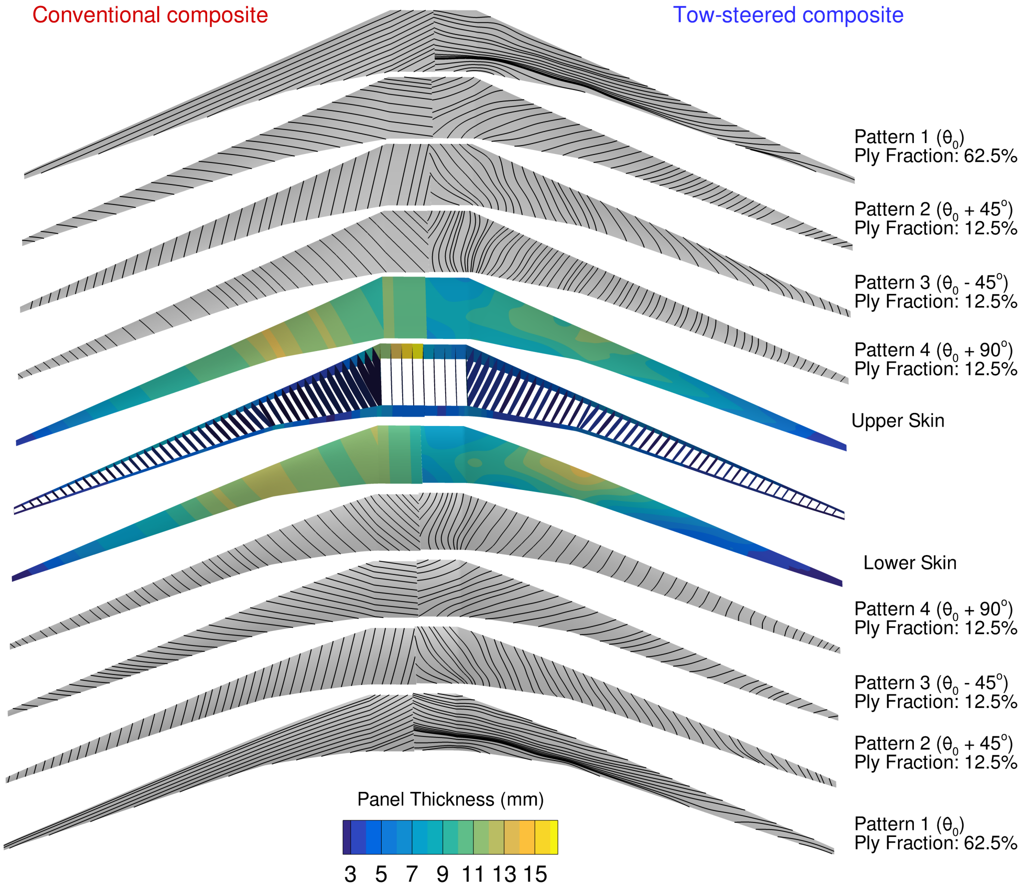
Conventional composite
Tow-steered composite
Pattern 1 (θ0)
Ply Fraction: 62.5%
Pattern 2 (θ0 + 45°)
Ply Fraction: 12.5%
Pattern 3 (θ0 - 45°)
Ply Fraction: 12.5%
Pattern 4 (θ0 + 90°)
Ply Fraction: 12.5%
Upper Skin
Lower Skin
Pattern 4 (θ0 + 90°)
Ply Fraction: 12.5%
Pattern 3 (θ0 - 45°)
Ply Fraction: 12.5%
Pattern 2 (θ0 + 45°)
Ply Fraction: 12.5%
Pattern 1 (θ0)
Ply Fraction: 62.5%
Panel Thickness (mm)
3
5
7
9
11
13
15

Figure 4: Exploded view of conventional composite plies (left) and tow-steered composite plies (right) for wingboxes using the developed parameterization.

4.1. *Laminate Failure*

We ensure that each panel in the wingbox model is adequately sized with respect to material failure for each structurally critical flight condition. We model the laminate failure using the maximum strain criterion,

$$\max\left\{\frac{\epsilon_1}{\epsilon_{1_t}}, \frac{\epsilon_1}{\epsilon_{1_c}}, \frac{\epsilon_2}{\epsilon_{2_t}}, \frac{\epsilon_2}{\epsilon_{2_c}}, \frac{\gamma_{12}}{\gamma_{12_s}}, -\frac{\gamma_{12}}{\gamma_{12_s}}\right\}, \tag{1}$$

where ϵ_1, ϵ_2, and γ_{12} are the in-plane tangential, transverse, and shear strains, respectively, relative to the local fiber direction, and

$$\epsilon_{1_t} = \frac{X_t}{E_1}, \qquad \epsilon_{1_c} = \frac{X_c}{E_1}, \qquad \epsilon_{2_t} = \frac{Y_t}{E_2}, \qquad \epsilon_{2_c} = \frac{Y_c}{E_2}, \qquad \gamma_{12_s} = \frac{S}{G_{12}},$$

where X_t and X_c denote the tensile and compressive ply strengths in the fiber direction, respectively, and Y_t and Y_c are the strengths in the transverse direction. The in-plane shear strength is denoted by S. The values for these material properties are listed in Table 2. Due to the difficulties introduced by the discontinuous nature of the maximum function in Equation (1), we approximate it using the Kreisselmeier–Steinhauser (KS) aggregation function [36, 37].

The failure constraint is applied using a first-ply failure criteria, where no ply in the laminate is permitted to fail. The failure criteria are applied conservatively by evaluating Equation (1) at the centroid of each CSM element for the outermost plies. Because the stacking sequence is never specified in the laminate parameterization scheme, the calculation is performed in the local fiber direction for each of the four tow patterns. The failure value for each pattern at each location is then aggregated one final time, again using another KS function, into a single scalar value for each structural component (ribs, spars, and skins). The value for each component is then provided to the optimizer as a constraint.

4.2. Panel Buckling

We also constrain the wingbox panels from buckling in the optimization problem formulation. The buckling behavior is approximated through a simplified panel-level buckling analysis of the stiffened panels applied to every wingbox component. This buckling analysis considers both longitudinal and shear buckling modes through several different buckling mechanisms, including inter-stiffener panel buckling, stiffener buckling, and overall panel buckling (including skin and stiffeners). Each panel is treated as simply supported at the rib attachment points, and the panel length set to the rib pitch. Due to the high aspect ratio of the skin panels, the second panel dimension in the chord direction is approximated as being infinite. This allows the critical buckling loads in this direction, $N_{2,cr}$, to be neglected. Lastly, panel curvature effects are neglected.

The first step of the procedure is to compute the critical buckling loads for each mechanism—compression ($N_{1,cr}$) and shear ($N_{12,cr}$)—for each panel. These critical loads are dependent on the local stiffness and geometric properties and are calculated using the approach of Stroud and Agranoff [38], later applied by Kennedy et al. [39, 40]. In this approach, each mode is treated separately and computed based on the formula summarized in Table 4. Here, EI_s is the effective bending stiffness of the panel, while D_1, D_2, and D_3 are the overall longitudinal, transverse, and twist bending stiffness of the smeared panel. D_{11}, D_{22}, D_{12}, and D_{66} are components of the bending stiffness matrix, $\boldsymbol{D}$, for the skin laminate and relate the mid-plane bending curvatures of the laminate, κ, to the moment resultants, M, as follows:

$$\begin{bmatrix} M_{xx} \\ M_{yy} \\ M_{xy} \end{bmatrix} = \begin{bmatrix} D_{11} & D_{12} & D_{16} \\ D_{12} & D_{22} & D_{26} \\ D_{16} & D_{26} & D_{66} \end{bmatrix} \begin{bmatrix} \kappa_{xx} \\ \kappa_{yy} \\ \kappa_{xy} \end{bmatrix}. \tag{2}$$

Next, the local running load in each element, N_1 and N_{12}, are computed and used to evaluate the buckling constraint for each buckling mechanism based on an interaction criteria:

$$B(N_1, N_{12}) = \frac{N_{12}^2}{N_{12,cr}^2} + \frac{N_1}{N_{1,cr}} \leq 1. \tag{3}$$

This results in a conservative envelope that is applied to every element in the panel. This method has the advantage of being computationally inexpensive relative to performing a full buckling eigenvalue analysis for each panel. Like the failure constraints, the buckling constraints are evaluated at the centroid of every element. Finally, these element constraints are aggregated over each component group using a KS function.

Table 4: Critical loads for overall and skin buckling [38].

	Overall buckling	Skin buckling
$N_{1,cr}$	$\frac{\pi^2 E I_s}{s_p L_x^2}$	$\frac{2\pi^2}{s_p^2}\left(\sqrt{D_{11}D_{22}} + D_{12} + 2D_{66}\right)$
$N_{12,cr}$	$\xi = \frac{\sqrt{D_1 D_2}}{D_3}$	$\xi = \frac{\sqrt{D_{11}D_{22}}}{D_{12} + 2D_{66}}$
If $\xi > 1$	$\frac{4}{L_x^2}(D_1^3 D_2)^{0.25}\left(8.125 + \frac{5.045}{\xi}\right)$	$\frac{4}{s_p^2}(D_{11}^3 D_{22})^{0.25}\left(8.125 + \frac{5.045}{\xi}\right)$
If $\xi \leq 1$	$\frac{4}{L_x^2}\sqrt{D_1 D_3}\left(11.7 + 0.532\xi + 0.938\xi^2\right)$	$\frac{4}{s_p^2}\sqrt{D_{22} 2(D_{12} + 2D_{66})}\left(11.7 + 0.532\xi + 0.938\xi^2\right)$

5. AFP Manufacturing Constraints

To ensure that the resulting optimized tow-steered layups are physically realizable with modern-day AFP machines, several manufacturing restrictions are considered in this work. The first is a bound on the minimum turning radius, R_{min}, of the tow paths for each tow pattern in the skins. This value is typically specified by the manufacturer to prevent the tow from puckering or twisting out of plane as it is being laid down by the machine, particularly in highly curved regions of the tow path. Smaller values of R_{min} can often be achieved by using narrower tows; however, this may lead to longer manufacturing time for the same layup area.

The second restriction is on the minimum cut and add lengths for the AFP machine tows. When the tows are laid down for a ply by the AFP machine, gaps or overlaps may occur between adjacent tow paths. To keep the layup smooth, the machine is often preprogrammed to add or cut tows in regions where the gap or overlap sizes, respectively, exceed a specified value expressed as a percentage of tow width. The machine has a minimum cut length for the tow (L_{cut}), which is limited by the distance between the AFP tow placing head and cutting mechanism. The minimum add length (L_{add}) defines the minimum length of tow for two adjacent tow paths that must be laid before the machine may add a tow between the gap of the previous two. Unlike the minimum cut length value, the add length is not limited by the dimensions of the AFP machine and, as such, is at the designer's discretion. The definition of each of these lengths is illustrated in Figure 5. Tow patterns featuring smaller cut and add lengths require more frequent cutting and repositioning of the tows in the layup process, leading to a higher manufacturing cost and time. To increase

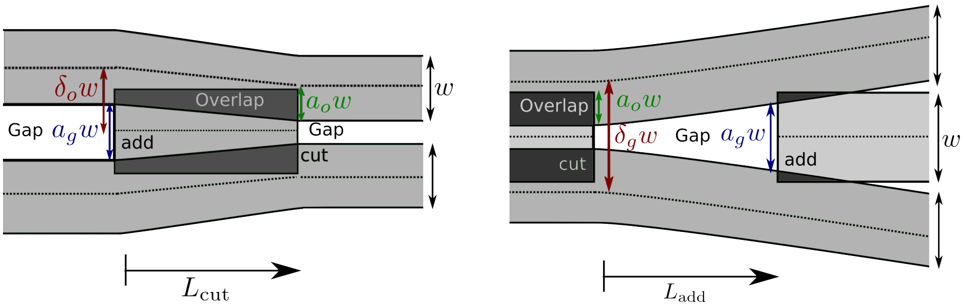

Minimum cut length

Minimum add length

Figure 5: Definition of tow cut and add length (reproduced from Brooks and Martins [41]).

the manufacturability of the optimized design, we must constraint each of these values in the optimization.

The final restriction is on how quickly the number of plies can vary spatially through the laminate. This is typically constrained in the design process to prevent stress concentrations from occurring in regions featuring a large decrease in the number of plies.

For the minimum tow-path turning radius and cut/add length constraints, we use the relationships derived in our previous work [41], where we showed that the tow paths of each ply of a tow-steered layup can be defined as the streamlines of a 2D unit vector field as,

$$\vec{v}(\theta) = \cos(\theta(x, y))\,\hat{\mathbf{i}} + \sin(\theta(x, y))\,\hat{\mathbf{j}}. \tag{4}$$

Through this relationship and with further derivation, we showed that the minimum tow-path turning radius and tow-path cut/add lengths can be bounded by constraining the magnitude of the vector field curl, $\kappa \equiv (\nabla \times \vec{v}) \cdot \hat{\mathbf{k}}$, and divergence, $\psi \equiv \nabla \cdot \vec{v}$, respectively, as shown below:

$$-\frac{1}{R_{\text{min}}} \leq \kappa \leq \frac{1}{R_{\text{min}}}, \qquad -\frac{\ln\left(\frac{1+a_g}{2(1-a_o)}\right)}{L_{\text{cut}}} \leq \psi \leq \frac{\ln\left(\frac{1+a_g}{2(1-a_o)}\right)}{L_{\text{add}}}, \tag{5}$$

where a_g and a_o are the gap and overlap cut sizes for the AFP machine in percent tape width, respectively. We can bound the ply drop rate by constraining the thickness gradient of the smeared laminate:

$$||\nabla t_p(x, y)|| \leq ||\nabla t_0||. \tag{6}$$

To constrain the tow-path turning radius, cut/add length, and ply drop rate, we use a KS aggregation function once again. This is accomplished by computing the tow-path curl and divergence for each pattern, as well as the panel thickness gradient at each node on the skins of the CSM model, and then aggregating these into three scalar values (one for each constraint) over each wingbox skin panel.

6. Bend-twist Coupling Quantification

When comparing the amount of passive load alleviation introduced into the design through material bend-twist coupling, it is useful to define a metric to measure the local degree of coupling in the wing. It is well-known from classical lamination theory that the bend-twist coupling in a laminate structure is closely related to the laminate bending stiffness matrix, $\boldsymbol{D}$. The degree of spanwise bend-twist coupling is determined by the magnitude and sign of the off-diagonal term, D_{16}, in Equation (2). The typical way of increasing this term is by using increasingly unbalanced ply orientations (i.e., unequal number of $+\theta$ and $-\theta$ plies) in the laminate layup.

Shirk et al. [42] introduced the following non-dimensional coupling parameter to measure the magnitude of this term:

$$\psi_1 = \frac{D_{16}}{\sqrt{D_{11} D_{66}}}. \tag{7}$$

This parameter was originally derived for the aeroelastic analysis for a cantilevered composite plate. We extend this idea for the case of a thin-walled wingbox by treating it as a "sandwich" structure, allowing us to compute the effective bending stiffness matrix of the wingbox through-depth cross-section based on the stiffness matrices of the upper and lower skin panel pairs along the span of the wingbox using

$$\boldsymbol{D}^{\text{eff}} = \left(\frac{d}{2}\right)^2 (\boldsymbol{A}_u + \boldsymbol{A}_l)\,, \tag{8}$$

where $\boldsymbol{A}_u$ and $\boldsymbol{A}_l$ are the membrane stiffness matrices for each spanwise pair of upper and lower skin panels, respectively, and d is the local wingbox depth at each location, as illustrated in Figure 6. In this calculation, we neglect the effect of the stiffeners, spars, and ribs. This is acceptable, since we only want a metric that measures the bend-twist coupling added to the wing due to the directional stiffness tailoring of the skins, and the spars and ribs (which are made of balanced plies) make no contribution to this.

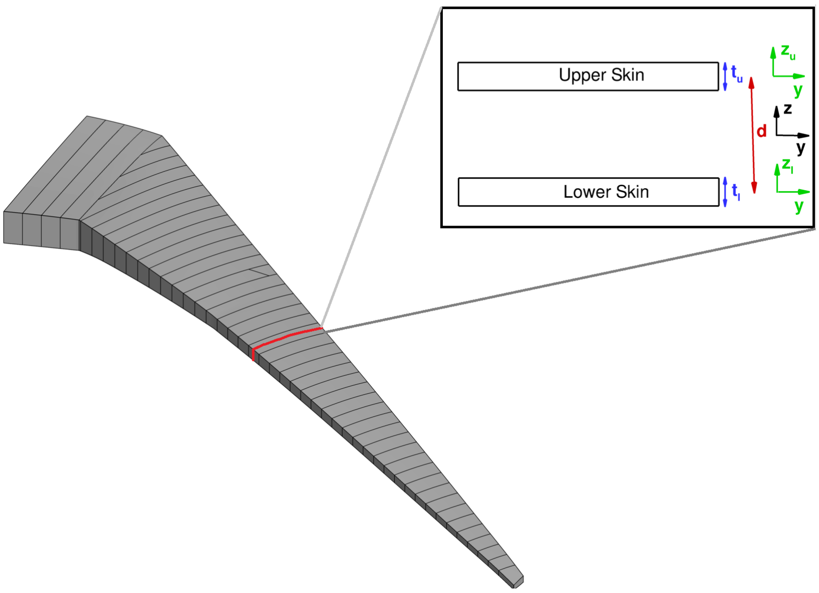

Figure 6: Cross-sectional view of typical wingbox skin panels

The components of $\boldsymbol{D}^{\text{eff}}$ can be substituted into Equation (7) to yield the bend-twist coupling parameter of the wing box,

$$\psi_1^{\mathrm{wb}} = \frac{A_{u_{16}} + A_{l_{16}}}{\sqrt{(A_{u_{11}} + A_{l_{11}})\,(A_{u_{66}} + A_{l_{66}})}}. \tag{9}$$

The effect of the wingbox depth, d, cancels out, so ψ_1^{wb} ultimately only depends on the components of the membrane stiffness of each skin panel, $\boldsymbol{A}_u$ and $\boldsymbol{A}_l$. Because the panel thickness and ply orientation in this study vary within the panel, and thus so do $\boldsymbol{A}_u$ and $\boldsymbol{A}_l$, the membrane stiffness for each panel is approximated by averaging the values in each panel. Computing the coupling parameter at each spanwise wingbox section allows us to identify regions of the wingbox design for which the optimizer is taking advantage of the additional aeroelastic tailoring offered by anisotropy.

7. Optimization Problem

As previously mentioned, the goal of this study is to provide insights into the aeroelastic benefits of tow steering when applied to wing design. To this end, a series of fuel burn minimization problems is first performed on the uCRM-9. We run optimizations with both a tow-steered and fixed-ply-orientation conventional composite wingbox design. The benefits of optimized tow-steered design are then compared against a conventional design where the optimizer is free to rotate the wingbox skin plies relative to the wing. Next, the tow-steered and fixed-ply-orientation conventional composite design optimizations are performed on the uCRM-13.5. Including this design provides insight into the benefits of tow steering for high-aspect-ratio wing designs that are more flexible. Finally, an aspect ratio study is performed for the uCRM-9 design, where the wing aspect ratio is fixed at several values (7.5, 9, 10.5, 12, and 13.5) and re-optimized using the tow-steered and fixed-ply-orientation conventional composite designs. This provides insight into how the design trends change as aspect ratio is increased.

Each optimization requires three aerostructural analyses: one cruise condition for evaluating the fuel burn performance, and two conditions for which the structural constraints are enforced—a -1.0 g push-over and 2.5 g pull-up maneuver condition. The lift of the cruise condition is set to be that of the nominal CRM ($C_L = 0.5$), while the lift of the maneuver conditions are based on the maximum takeoff weight (MTOW) of the aircraft. The parameters for these three conditions are listed in Table 5. In the remainder of this section, we describe the optimization problems by detailing the objective function, design variables, and design constraints.

Table 5: Optimization flight condition parameters.

Parameter	Cruise	2.5 g	−1.0 g
Mach number	0.85	0.64	0.64
Altitude (ft)	37 000	0	0
C_L or lift	0.5	2.5 · MTOW	−1.0 · MTOW

7.1. Objective

The objective for all optimizations is to minimize the fuel burn for a given range. The fuel burn is calculated using a rearranged form of the Breguet range equation,

$$\mathrm{FB} = \mathrm{ZFW}\left(\exp\left(\frac{R\, c_T}{V_\infty\,(L/D)}\right) - 1\right), \tag{10}$$

where ZFW, R, and c_T are the aircraft zero-fuel weight, design range, and thrust-specific fuel consumption, respectively, and V_∞ and L/D are the cruise speed and lift-to-drag ratio, respectively. The zero-fuel weight is defined as the total aircraft weight including payload and crew without the fuel required for the mission and is given by:

$$\mathrm{ZFW} = 1.25 \times W_{\mathrm{wing}} + W_{\mathrm{secondary}} + W_{\mathrm{fixed}} + W_{\mathrm{payload}} + W_{\mathrm{reserve}}, \tag{11}$$

where W_{wing} is the wingbox structural weight, $W_{\mathrm{secondary}}$ is the weight of non-structural masses associated with the wing (e.g., control surfaces, actuators, etc.), W_{fixed} is the weight of the aircraft structure without the wing (e.g., fuselage, tail), W_{payload} is the weight of the payload (e.g., passengers, luggage), and W_{reserve} is the weight of the reserve fuel. The only portion of this weight that the optimizer can affect is the wing structural weight, W_{wing}. A factor of 1.25 is added onto the wing structural weight predicted by the CSM model to account for the weight of overlaps and fasteners. The values of the constants used to compute the objective are listed in Table 6.

The fuel burn makes for a good multi-disciplinary objective function due to its dependence on both structural performance, through the zero-fuel weight, as well as aerodynamic performance, through L/D. In addition, its relationship to the direct operating cost of the aircraft makes it an appropriate metric for the aircraft performance.

Table 6: Aircraft sizing specifications

Parameter	Symbol	Value	Units
Design range	R	7 725	nm
Design payload	W_{payload}	34 000	kg
Reserve fuel	W_{reserve}	15 000	kg
Fixed weight	W_{fixed}	107 814	kg
Thrust specific fuel consumption	c_T	0.53	lb/(lbf · h)

7.2. Design Variables

The design variables can be divided into structural, geometric, and aerodynamic variables. We consider three different design parameterizations in this study: tow-steered composite (TS), fixed-ply-orientation conventional composite (C), conventional rotated-ply-orientation composite (CR), and tow-steered and conventional composite with different wing aspect ratios (TS-AR and C-AR, respectively). Each of these parameterizations, with the exception of TS-AR and C-AR, use the same geometric and aerodynamic design variables but differ in the structural variables they use. The design variables used for each design case are summarized in Table 7. All possible design variables are illustrated in Figure 7.

The first of the structural variables is the panel thickness. These are set using 120 B-spline control points distributed over each skin, 20 control points distributed over each spar, and one variable for each rib. The structural variables also include the stiffener height, stiffener thickness, and panel length for each panel shown in Figure 7, for a total of 287 of each of these types of variables. The panel length variable is only used in the prediction of the analytical panel buckling formulas. In addition, all panels in each component (upper skin, lower skin, ribs, and spars) share a stiffener pitch variable, for a total of four. Finally, the tow-steered design parameterizations (TS and TS-AR) also include the tow-offset control point variable, θ_0^{cp}, on each skin, for a total of 240 additional variables. The main ply orientation in the skins for the conventional composite designs

Variable	Description	TS	C	CR	TS-AR	C-AR
$x_{\text{stiff thick}}$	Stiffener thickness (skin/spar/ribs)	238				
$x_{\text{stiff height}}$	Stiffener height (skin/spar/ribs)	238				
$x_{\text{stiff pitch}}$	Stiffener pitch (skin/spar/ribs)	4				
$x_{\text{panel length}}$	Panel length (skin/spar/ribs)	238				
$x_{t^{\text{cp}}}$	Panel thickness control points (skin/spar)	280				
x_{ribs}	Panel thickness (ribs)	49				
$x_{\theta_0^{\text{cp}}}$	Tow offset control points (skin)	240	0	2	240	0
x_{shape}	FFD control points	240				
x_{twist}	Wing twist	8				
x_{chord}	Chord scaling	0	0	0	1	1
x_{span}	Span	0	0	0	1	1
x_{sweep}	Sweep	0	0	0	1	1
x_{α_i}	Angle of attack for each case	3				
x_{tail}	Tail trim angle for each case	3				
	Total design variables	**1541**	**1301**	**1303**	**1544**	**1304**

Table 7: Optimization problem design variables for tow-steered composite (TS), fixed-ply-orientation conventional composite (C), conventional rotated-ply-orientation composite (CR), and tow-steered and conventional composite with varying wing aspect ratio (TS-AR and C-AR, respectively).

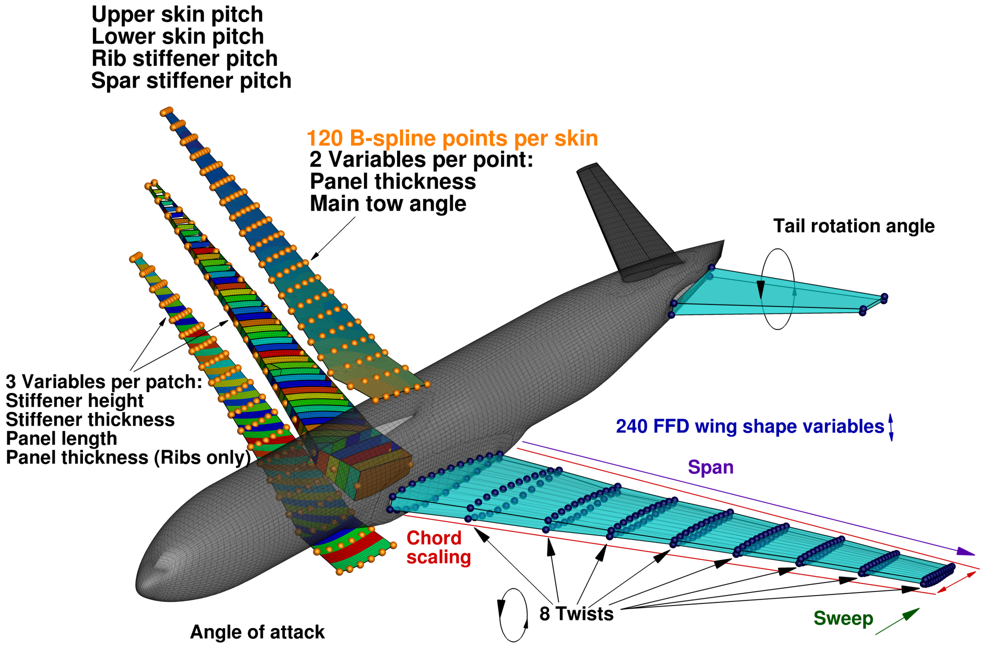
Upper skin pitch
Lower skin pitch
Rib stiffener pitch
Spar stiffener pitch
120 B-spline points per skin
2 Variables per point:
Panel thickness
Main tow angle
Tail rotation angle
3 Variables per patch:
Stiffener height
Stiffener thickness
Panel length
Panel thickness (Ribs only)
240 FFD wing shape variables
Span
Chord
scaling
Angle of attack
8 Twists
Sweep

Figure 7: Possible design variables for optimization problems.

(C and C-AR) are forced to remain parallel to the leading edge of the wing. This restriction is relaxed for the conventional rotated design (CR) by setting one tow-offset design variable for each skin. This gives the optimizer the freedom to rigidly rotate the layup of each skin with respect to the wing. This means that, for example, if the tow-offset angle is set to 10° for the upper skin, a layup of [0°, 45°, −45°, 90°] plies will turn into a layup of [10°, 55°, −35°, 100°] plies.

The geometric variables are parameterized using a free-form deformation (FFD) volume approach [43, 44]. In this approach, the wing and internal structure are enclosed by a volume whose surface includes a number of control points. As each control point is moved in space, any geometry inside of the volume is deformed in a similar fashion. The FFD volume used for this study is shown on the right in Figure 7. The optimizer is given freedom to control the wing cross-sectional shape by moving each of the 240 control points in the vertical (z) direction. The optimizer can control the wing twist at eight spanwise locations by rotating each chordwise segment of control points. The last set of geometric design variables control the wing planform and are only active for the variable aspect ratio problems (TS-AR and C-AR). These design variables consist of one chord variable, which uniformly scales the chord of all spanwise cross-sections, the wing span, and a wing sweep that shears the wing tip in the stream-wise direction.

The two aerodynamic design variables are the angle of attack and the horizontal tail incidence for each flight condition. These variables ensure the optimizer can satisfy the lift and moment constraints to trim the aircraft at each flight condition. The tail rotation is controlled by a small FFD volume surrounding the tail geometry.

7.3. Constraints

The design constraints can also be broken down into structural, geometric, and aerodynamic constraints. The constraints for each case are summarized in Table 8.

We add the structural constraints to ensure that the resulting optimized wingbox design is adequately sized and manufacturable. The first set of constraints consist of the aggregated material failure and buckling constraints, discussed in Section 4. The failure constraint is applied only on the 2.5 g maneuver, since this condition is the most restrictive in terms of stress. The buckling constraint is applied to both the −1 g and 2.5 g conditions to ensure that both the skins, ribs, and spars are sized for buckling. A safety factor of 1.5 is placed on both the failure and buckling constraints to provide the necessary margin of safety as required by Federal Aviation Regulations Part 25 [45]. Linear adjacency constraints are enforced on the stiffener height and thickness variables to ensure that they do not vary too abruptly between adjacent panels. The last set of structural constraints pertain to the AFP manufacturing constraints described in Section 5. These include a constraint on the panel thickness gradient of the skins and spars used to limit the ply drop rate. The maximum thickness gradient value, $||\nabla t_0||$, is set to 1.3 mm/m, which corresponds to a ply drop rate of roughly 10 plies per meter. The tow-steering-specific manufacturing constraints are applied only to the tow-steered cases (TS and TS-AR). These include a constraint on the tow-path turning radius of each steering pattern, which is constrained to a minimum turning radius, R_{min}, of 70 in. This value is recommended by AFP technicians at Aurora Flight Sciences for a 0.5 in-wide prepreg tape. As mentioned previously, while more aggressive values of tow-path curvature could be pursued through the use of narrower prepreg tape, this results in an increase in layup time and manufacturing cost. The final manufacturing constraint, the minimum tow cut and add lengths, are constrained to a value of $L_{\text{cut}} = L_{\text{add}} = 1$ m, assuming a 50% gap/ 50% overlap rule ($a_g = a_o = 0.5$). This value was determined to be reasonable based on the dimensions of the uCRM wing structures.

We also enforce geometric constraints that relate to the physical restrictions of a realistic wing design. The first of these constraints prevents the cross-sectional depth at the leading-edge radius from decreasing. This is mainly to maintain the aircraft's high-lift performance, a flight case which we do not consider directly in the optimization. We also prevent manufacturing and handling issues by constraining the trailing-edge and spar cross-sectional thicknesses. We constrain the FFD shape variables from moving the camber line at the leading and trailing edge of the wing. These constraints prevent the shape variables from twisting the wing and guarantee that the twist and shape variables are independent. We enforce a volume constraint on the fuel bays inside the wing to ensure that there is enough space for the fuel required for the mission, computed by Equation (10), in addition to the reserve fuel. Next, a consistency constraint ensures that the panel length variables used in the panel buckling calculations match the physical dimensions of each panel. Additional geometric equality constraints are also enforced on the variable planform cases, TS-AR and C-AR. This includes a constraint on the aspect ratio of the wing. An optimization is run for each of these cases with an aspect ratio of 7.5, 9, 10.5, 12, and 13.5. A constraint is forced on the value of both the wing quarter-chord sweep, $\Lambda_{c/4}$, and reference area, S_{ref}, to force the wing to retain the original values of the uCRM-9. These constraints ensure that no additional bend-twist coupling is added to the design through sweep and that designs maintain the same wing loading, respectively. These three constraints are enough to uniquely prescribe the planform for each aspect ratio.

Next, we have constraints that enforce steady level flight at each analyzed flight condition. We have a lift constraint for each flight condition that matches the conditions specified in Table 5. We also have constraints enforcing that the pitching moment of the aircraft about its center of gravity must be zero for each flight condition.

8. Results

We now present the results for all of the design optimization studies. First, we demonstrate the benefits of tow steering for a typical wide-body transport aircraft by performing a tow-steered and fixed-ply conventional composite design optimization on the uCRM-9. The tow-steered optimized design is then compared against another optimized conventional design in which the optimizer is given the freedom to rotate the skin plies. Then, the effect of tow steering on high-aspect-ratio wing design is explored by performing conventional and tow-steered composite design optimizations on the uCRM-13.5. Finally, we investigate the trend with wing aspect ratio by re-optimizing the tow-steered and conventional composite wing designs with several different aspect ratios.

8.1. uCRM-9 Optimization

Here, we analyze the results of the first three optimization cases based on the uCRM-9 model. The convergence history of the optimization objective and feasibility (i.e., the magnitude of total constraint violation) for each uCRM-9 optimized case is shown in Figure 8. Each optimization is run for 48 hours with a total of 300 processors (100 processors per flight condition). From these optimization histories, we can see that the designs converge gradually before reaching the time limit. While further benefits in each design might be found by continuing the optimization for more iterations, the subsequent improvements were deemed to be small by the exit of each optimization.

Function	Description	TS	C	CR	TS-AR	C-AR
$\mathrm{KS}_{\text{fail}} < 1.0$	2.5 g Material Failure	4				
$\mathrm{KS}_{\text{buckling}} < 1.0$	2.5 g and −1.0 g Buckling	6				
$\left\lvert x_{\text{stiff height}_i} - x_{\text{stiff height}_{i+1}} \right\rvert \leq 0.0005$	Stiffener height adjacency	183				
$\left\lvert x_{\text{stiff thick}_i} - x_{\text{stiff thick}_{i+1}} \right\rvert \leq 0.0005$	Stiffener thickness adjacency	183				
$\left\lvert x_{\text{stiff thick}} - x_{\text{panel thick}} \right\rvert < 0.0025$	Maximum stiffener-panel difference	238				
$\mathrm{KS}_{\Vert \nabla t_p \Vert} < \Vert \nabla t_0 \Vert$	Panel thickness gradient	183				
$-\frac{1}{R_{\min}} < \mathrm{KS}_{\kappa} < \frac{1}{R_{\min}}$	Minimum tow-path turning radius	96	0	0	96	0
$-\frac{\ln\left(\frac{1+a_g}{2(1-a_o)}\right)}{L_{\text{cut}}} < \mathrm{KS}_{\psi} < \frac{\ln\left(\frac{1+a_g}{2(1-a_o)}\right)}{L_{\text{add}}}$	Minimum tow cut/add length	96	0	0	96	0
$t_{LE}/t_{LE_{init}} \geq 1.0$	Leading-edge radius	20				
$t_{TE}/t_{TE_{init}} \geq 1.0$	Trailing-edge thickness	20				
$(t/c)_{\text{TE spar}} \geq 0.80(t/c)_{\text{TE spar}_{init}}$	Minimum trailing-edge spar height	20				
$\Delta z_{\text{TE,upper}} = -\Delta z_{\text{TE,lower}}$	Fixed trailing edge	8				
$\Delta z_{\text{LE,upper}} = -\Delta z_{\text{LE,lower}}$	Fixed leading edge	8				
$V - V_{\text{fuel}} \geq 0.0$	Minimum fuel volume	1				
$L_{\text{panel}} - x_{\text{panel length}} = 0$	Target panel length	238				
$\mathrm{AR} = [7.5,\ 9,\ 10.5,\ 12,\ 13.5]$	Aspect ratio	0	0	0	1	1
$\Lambda_{c/4} = 34.8^\circ$	Quarter-chord sweep	0	0	0	1	1
$S_{\text{ref}} = 191.8\,\mathrm{m}^2$	Reference area	0	0	0	1	1
$C_L = 0.5$	Cruise lift conditions	1				
$L_i = n_i\,\mathrm{TOGW}$	Maneuver lift conditions	2				
$C_{m_y}^{i} = 0$	Trimmed flight	3				
	Total constraints	**1316**	**1124**	**1124**	**1319**	**1127**

Table 8: Optimization problem constraints for tow-steered composite (TS), fixed-ply-orientation conventional composite (C), conventional rotated-ply-orientation composite (CR), and tow-steered and conventional composite with varying wing aspect ratio (TS-AR and C-AR, respectively).

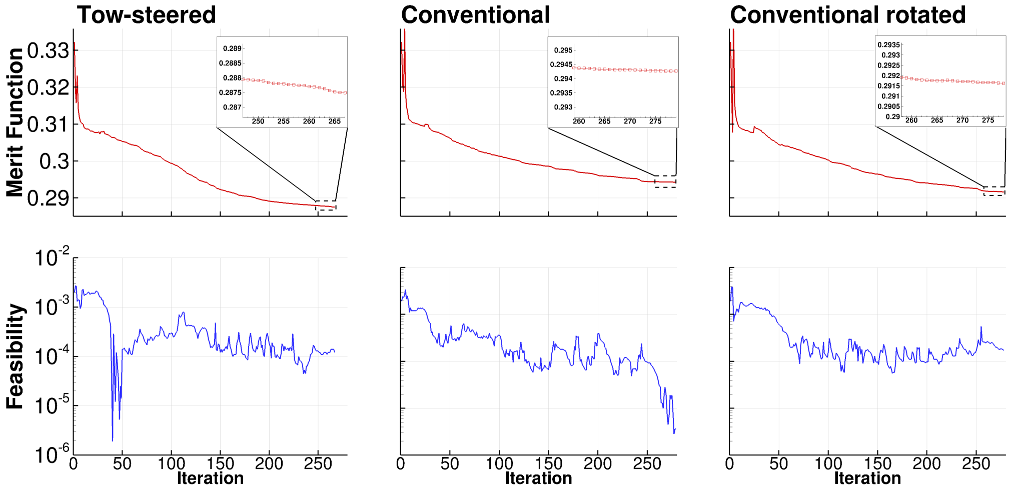

Figure 8: Optimization convergence histories for each uCRM-9 case.

8.1.1. *Conventional Versus Tow-steered Composites*

The resulting designs from the fixed-ply conventional and tow-steered composite optimizations are summarized in Figure 9, which compares the aerodynamic and structural performance of the tow-steered (left) and conventional (right) composite wing designs. In the upper left corner of this figure, we show the aerodynamic pressure distribution on the wing at cruise as well as several key performance metrics for both designs. Just below this is a front view of the aircraft, showing the relative deflection of the wing at each flight condition. In the bottom left corner, we show the wingbox structural information. This includes a plot showing the panel thickness distribution for each design and the tow paths for the main tow patterns for each skin. This structural information also includes contours for the failure and buckling constraints on the wing skins for the 2.5 g and -1 g maneuver conditions.

On the right side of the figure, we show various spanwise metrics measuring the passive load alleviation and bend-twist coupling of each design. Starting from the top, we have the normalized lift distribution for the cruise and 2.5 g flight conditions, which represents the distributed lift per unit span over either aircraft. Below this, we have the aeroelastic spanwise twist distribution for both wing designs. Finally, in the bottom right, we have a plot of the spanwise non-dimensional bend-twist coupling parameter, ψ_1^{wb}, which was introduced in Section 6.

From Figure 9, we see 2.3% and 2.5% improvements in the design fuel burn and MTOW, respectively, of the tow-steered design relative to the conventional composite one. The optimizer accomplishes this through a significant reduction in structural weight (24%) for almost no aerodynamic penalty, as seen in the L/D performance of both designs (less than 0.15% difference). To see how this is achieved, we examine the normalized lift distributions for each design. What we find is that both designs achieve a more elliptical lift distribution at cruise, which minimizes the induced drag of the aircraft and improves the L/D. Where the two designs differ is in the passive load alleviation for the maneuver flight conditions. For these conditions, the tow-steered wing is able to shift more of the lift distribution inboard at the 2.5 g maneuver condition. This means that the tow-steered design can more effectively reduce the bending moment in the wing for this condition, allowing the optimizer to reduce the wingbox weight, most noticeably at the root and at the spanwise position of the trailing-edge break. This trend is similar to that observed by Stodieck et al. [15] when comparing a structural-weight-minimized tow-steered and conventional composite CRM wing design. The wing weight reduction of 24% found in this case is notably larger than the 12% found by Stodieck et al. [15]. The larger improvement is likely due to the carry-through segment of the wingbox, where weight improvements of the tow-steered design are greatest, since they did not include this segment in their optimization. The additional load alleviation contributes only in part to the lower structural weight seen on the tow-steered design. As will be seen in the following section, there is another factor associated with the local tailoring of the load paths in the structure.

This additional load alleviation can be explained by examining the spanwise twist distribution of both wings. What we find is that the twist distribution for both designs is nearly identical for the cruise condition. Again, this is due to the fact that both designs try to get close to an elliptical lift distribution. The two designs differ in that there is more spread in the aeroelastic twist deformation about the cruise condition for the tow-steered design. This allows the tow-steered structure to aeroelastically twist the wing tips down even further at the maneuver condition, leading to the additional passive load alleviation benefit seen in the lift distribution. The tow-steered design has 2.1° more washout at the wing tip for the 2.5 g maneuver than the conventional composite design.

Examining the spanwise bend-twist coupling due to the wing skins (bottom right in Figure 9), the coupling increases along the span before reaching the maximum value and dropping off rapidly toward the tip. The reason for this sudden decrease in the use of coupling near the tips is that, as we approach the wing tips and the aeroelastic deflections increase, there is local loading and therefore a diminishing ability to tailor the load. These two factors counteract each other and lead to a peak in the effectiveness of the coupling occurring slightly before the tip of the wing.

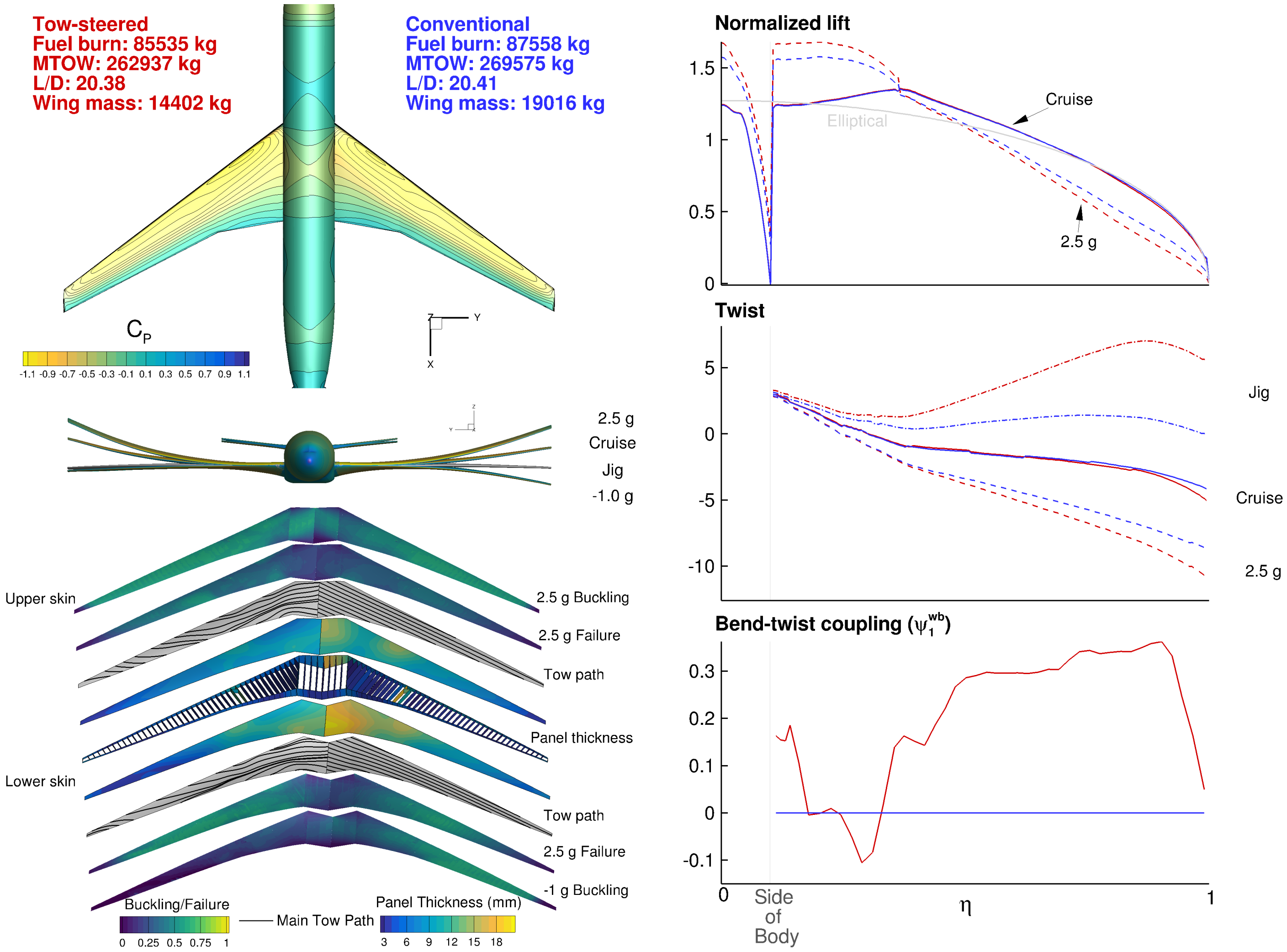

Figure 9: Comparison of the uCRM-9 aerostructural optimizations using tow-steered (left) versus conventional (right) composites.

Near the fuselage junction of the wing, the coupling initially drops and becomes negative. This is because the small displacements in this region limit the ability to tailor the structure aeroelastically in this region. Instead, the optimizer focuses on tailoring the strength of the structure in this region.

The tow-steered design exhibits a higher twist in the wing jig shape compared to the conventional composite (mid-right in Figure 9). This is to compensate for the increased bend-twist coupling of the tow-steered design, which induces more aeroelastic twist on the outboard of the wing for both the cruise and maneuver conditions. In general, the change in aeroelastic twist in the 2.5 g maneuver due to this increase in coupling is larger than that seen on the cruise shape. The optimizer therefore needs to increase the jig twist on the wing to keep the normalized lift distribution for the cruise case closer to elliptical.

The source of this additional bend-twist coupling can be found by analyzing the main tow paths for the tow-steered wing. By comparing the two wingbox designs, we find that the most noticeable difference is that the tow-steered optimized design sweeps the tow paths forward toward the tip of the wing. The use of swept-forward plies in this region leads to the increase in bend-twist coupling at the tip of tow-steered design in Figure 9. Thus, the tow paths in this region of the tow-steered structure are driven by load manipulation through aeroelastic tailoring. This use of unbalanced plies toward the wing tips is similar to trends that were found by Stodieck et al. [15] and Stanford and Jutte [16].

In contrast to the wing tips, the tow paths of the tow-steered skins near the root seem to be driven by structural tailoring of the load paths and directional strength. Note that the wingbox is structurally supported by the boundary conditions at the symmetry plane (clamped) and wing-fuselage intersection (no vertical displacement). For the portion of the skins inside the fuselage, the optimizer rotates the tow paths to be perpendicular to its supports, maximizing the compression strength of the skins.

The structural performance of both wingboxes provides additional information about the structural sizing for the maneuver cases. For the 2.5 g maneuver, we see that due to the compression in the upper skins, they are almost entirely sized by the buckling constraint for both designs (bottom left of Figure 9). For this flight condition, the failure constraint also drives the sizing of most of the lower skins for both designs. Despite the fact that the region for both designs where these constraints are active is largely the same, the tow-steered structure is noticeably thinner near the root and trailing-edge break on both the upper and lower skins. In the tow-steered design, the leading-edge spar is also noticeably thinner near root of wing, despite the fact this component is not tow-steered. These results demonstrate the ability of tow steering to redistribute loads in critical structural components through aeroelastic and structural tailoring, even if those components are not steered themselves. These differences account for the reduction in structural weight cited earlier.

Finally, we assess how much the manufacturing constraints introduced in Section 5 (minimum turning radius and cut/add length) limit the performance of the tow-steered optimized design. The minimum turning radius and cut/add length can be related to the tow-path curvature and divergence, respectively, through the inequalities provided in Equation (5). Substituting in the values specified in Section 7.3 gives the corresponding constraint bounds on the divergence and curvature used for the optimization: $|\psi| < 0.41\,\mathrm{m}^{-1}$, $|\kappa| < 0.56\,\mathrm{m}^{-1}$.

By plotting the tow-path divergence and curvature for each pattern of tow-steered design in Figure 10, we can find where each constraint is active. For conciseness, we only include the tow patterns corresponding to the upper skin in Figure 10; however, the lower skins have a similar constraint activity. Regions featuring higher tow-path divergence magnitude feature more rapid propagation of gaps and overlaps in the pattern, requiring more frequent tow cuts, while regions with higher curvature magnitude require tighter turning radii. From this figure, we can see that the most severe tow-path curvature and divergence occurs near the root of the wingbox, with a small amount near the tip. We also see that the locations and magnitudes of these constraint values differ slightly from pattern to pattern. From this, we can conclude that the manufacturing constraints are actively constraining the tow-steered design.

These results differ from those of Stodieck et al. [15], who found that the manufacturing constraints were active on the tow-steered design. This is likely due to the larger number of B-spline control points we used to parameterize the tow paths in the tow-steered skins. This highlights the importance of considering the manufacturing constraints for all patterns in the layup, not just the main tow pattern.

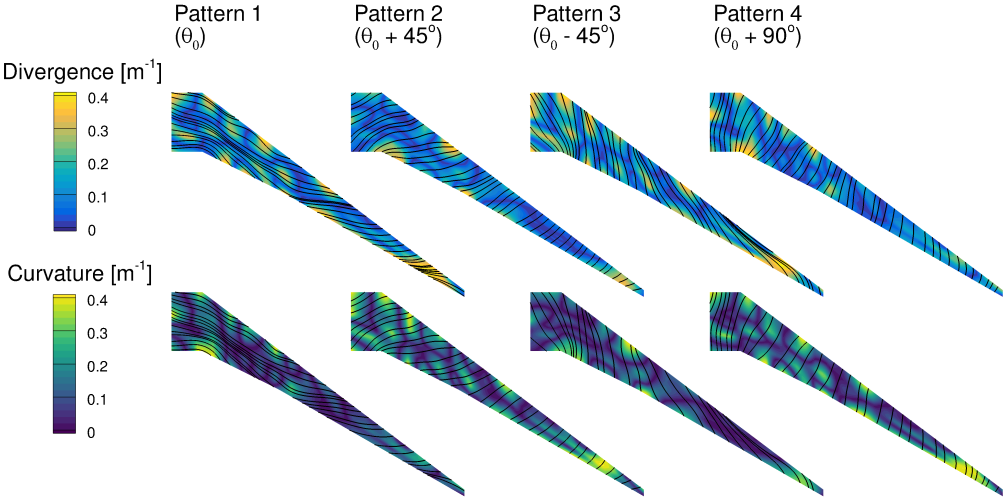

Figure 10: Tow-path curvature and divergence for upper skin of tow-steered optimized uCRM-9 design.

8.1.2. *Conventional Rotated Versus Tow-steered Composites*

We now relax the restriction on the conventional composite design by allowing the optimizer to rotate the wing skin plies. This is accomplished by giving the optimizer a single rotation design variable for each skin. This gives the optimizer the freedom to control the bend-twist coupling of the conventional wing and thus gives it the ability to aeroelastically tailor the design. The conventional optimization is run with these new design variables, and the results are compared to the tow-steered design.

From Figure 11, we can see that by rotating the skin plies of the conventional composite design, the optimizer has reduced the improvement margin in design fuel burn and MTOW to 1.4% and 1.5%, respectively, relative to the previous case. In addition, the structural weight improvement is now 15.7%. This decrease in relative performance margin is consistent with results found by Stodieck et al. [15] and Stanford and Jutte [16] when unbalanced plies were introduced to the conventional design. Based on the lift and twist distributions, it is clear that the optimizer is able to reduce this margin by increasing the load alleviation of the conventional design. In fact, the load alleviation performance for the 2.5 g maneuver is nearly identical between the two designs now. This means that any remaining benefit coming from the tow-steered design must be accounted for entirely by the local structural tailoring capability of the design. Using this information and the results from the previous case, we conclude that the benefit in fuel burn performance due to aeroelastic tailoring of the tow-steered design, when compared to the conventional design from the previous case, makes up roughly 0.9% of the previous 2.3% total. This means that the remaining 1.4% is due to local structural tailoring. Looking back at the tow paths of the conventional rotated design in Figure 11, we see that the optimizer makes the additional improvement in load alleviation possible by rotating the plies forward relative to the leading-edge spar of the wing, increasing the bend-twist coupling of the structure.

In the lift distribution for the 2.5 g maneuver of the conventional rotated design in Figure 11, we see a small dip in the lift distribution at roughly the 40% span location (indicated on plot). To explore the cause of this phenomenon, we plot aerodynamic streamlines of the flow on the upper surface of the wing in this region (see Figure 12). We also plot contour of a separation sensor, which is defined as the dot product of local air velocity with the freestream direction [46]. This reveals that the dip in the lift distribution in this region is due to a small region of separated flow on the upper wing surface. Comparing the airflow in this region for the conventional and tow-steered composite designs shows that this separated flow region is small for the conventional design, but grows larger for the tow-steered and conventional rotated designs. This is because as load alleviation is added into the design, the lift on the inboard of the wing must increase to offset the loss of lift at the tips. This increase in lift causes the airflow over the inboard of the wing to separate. This puts a practical upper limit on the maximum amount of load alleviation achievable by an aeroelastically tailored design. Because lower-fidelity aerodynamic models, such as panel methods and Euler-based CFD, do not model the physics required to predict separation, this highlights a benefit of using high-fidelity analysis in design optimization.

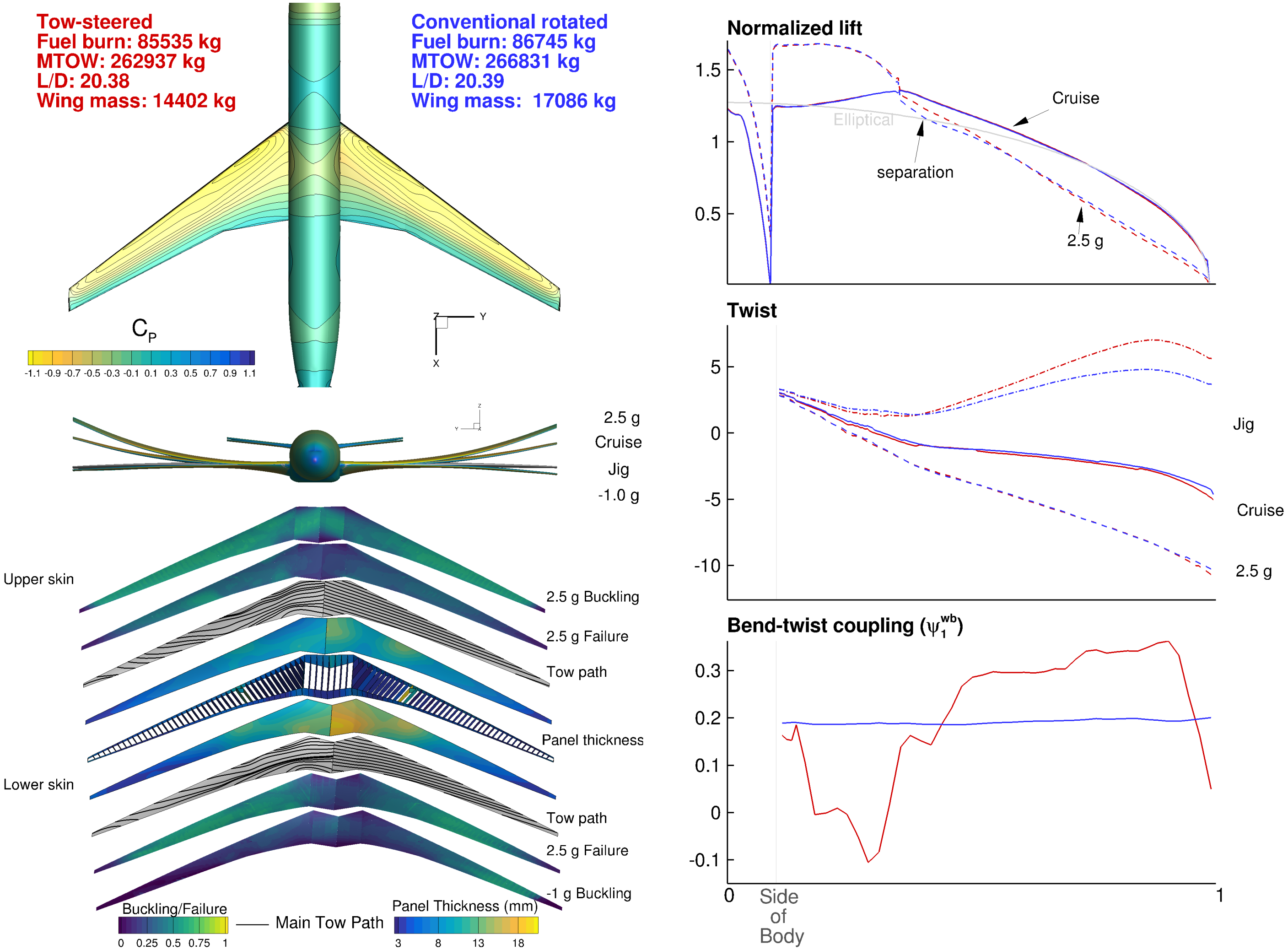

Figure 11: Comparison of the uCRM-9 aerostructural optimizations using tow-steered (left) and conventional rotated (right) composites.

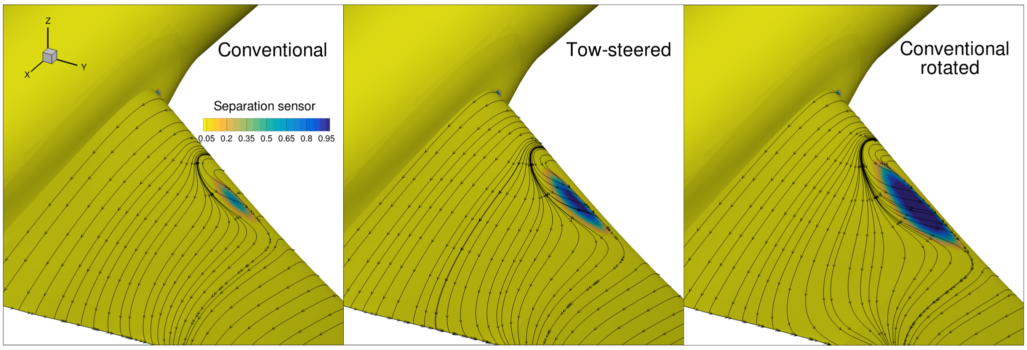

Figure 12: Separation sensor contour and airflow streamlines show region of separated flow on the 2.5 g for the tow-steered and conventional rotated composite designs.

8.2. *uCRM-13.5 Optimization*

We now present the optimization results for the higher-aspect-ratio uCRM-13.5 model. For this case, two additional aerostructural optimizations are run: one with a tow-steered wing design (TS), and one with a fixed-ply-orientation conventional composite design (CR). We plot and compare these results in Figure 13.

Comparing the performance of the uCRM-9 designs in Figure 11 with those of the uCRM-13.5 in Figure 13 reveals design trends expected of a higher-aspect-ratio wing design. Specifically, we see the fuel burn values for both uCRM-13.5 designs have decreased relative to their uCRM-9 counterparts. This is due to the reduction in induced drag owed to the larger span, which increases L/D. In addition, due to the larger moment arm on the wing structure, the structural weight increases for the uCRM-13.5 designs. From Figure 13, we see that adding tow steering to the uCRM-13.5 improves the fuel burn performance by 1.5% and MTOW by 1.5% relative to the conventional design. This benefit comes from the 14% reduction in weight achieved by the tow-steered design.

In the lift and twist distribution, we see that, unlike for the uCRM-9 case, the optimizer is not able to add any additional load alleviation to the tow-steered design. This means that the performance improvements seen on this design are entirely due to local structural tailoring. Upon closer examination of the two high-aspect-ratio designs in Figure 13, we see that while the spanwise twist distributions are nearly identical for the cruise and maneuver conditions, the initial jig twist of the tow-steered design is noticeably higher. This suggests that the bend-twist coupling of the tow-steered wing as measured from the jig (unloaded) to cruise wing shape is different than that measured from the cruise to 2.5 g maneuver shape. This same asymmetry in twist distribution can be seen in the comparison of the tow-steered and conventional uCRM-9 designs in Figure 11. The amount of bend-twist coupling seen on the 2.5 g maneuver condition is reduced relative to what otherwise should be expected, which suggests a nonlinear behavior. Because the structural model used in this work is linear, the cause of this behavior must be either from the aerodynamics or aeroelastic coupling.

By plotting the airflow on the upper surface of the wing for the 2.5 g maneuver, we find that, unlike for the uCRM-9 cases in Figure 12, the additional load alleviation is not being limited by separated flow at the root of the wing, so the cause is not aerodynamic.

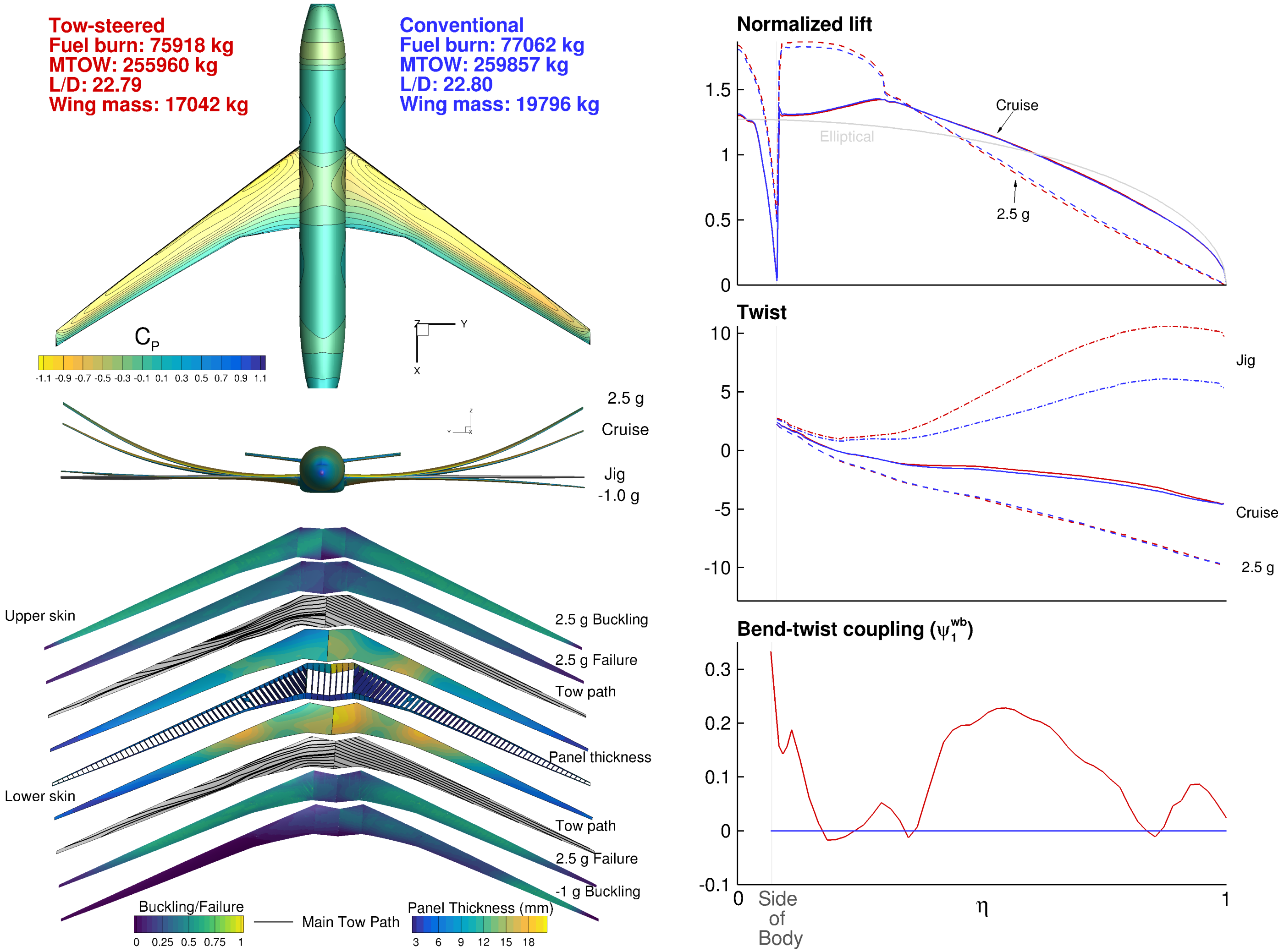

Figure 13: Comparison of the uCRM-13.5 aerostructural optimizations using tow-steered (left) and conventional (right) composites.

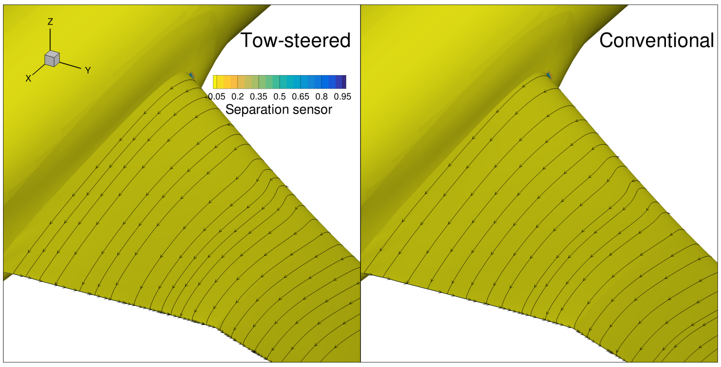

Figure 14: Separation sensor contour and airflow streamlines show no separated flow on uCRM-13.5 designs for 2.5 g maneuver.

If the cause of the lack of additional load alleviation in the tow-steered uCRM-13.5 model is not aerodynamic, the only remaining possible explanation is aeroelastic coupling. From aeroelastic theory, it is well known that as wings become more flexible, the control effectiveness of the ailerons is reduced and even reversed. Hence this aeroelastic phenomenon is called *control reversal*. This is because, when the aileron is deflected downward, while the local lift for this section of the wing increases, the torsional load on the wingbox increases as well. This increase in torsional load leads to an aeroelastic twisting of the wing—in this case nose-down twist—which counteracts the desired effect of the aileron. For this reason, aeroelasticians define the control effectiveness as the ratio of the response (increase in roll moment of the elastic wing due to the deployment of the aileron) to the response of a rigid wing.

The FFD twist parameterization used throughout this work can be thought of as behaving in an analogous fashion to a control surface. For example, as we twist the jig of the wing down at the wing tip using the FFD, the flying shape of the wing similarly experiences a decrease in twist at the tip. In response, the aeroelastic twist of the inboard of the wing increases due to the local reduction in load. This response counteracts some of the reduction in inboard bending moment expected from twisting the tip down with the FFD variable, and leads to a loss in sensitivity of the bending moment with respect to wing twist. This effect is illustrated in Figure 15, where the wing jig shape of the design is twisted down near the tip by twisting one of the spanwise FFD segments (shown in Figure 7) down. While this results in a net twisting down at this wing location for the 2.5 g wing shape, it is counteracted by a corresponding aeroelastic upward twist deformation farther inboard due to the change in load at the tip. This effect leads to a decrease in the sensitivity of twist in this location for the maneuver condition.

To quantify the twist sensitivity, similarly to the aileron effectiveness, we define the effectiveness of each spanwise FFD twist variable, x_{γ_i}, as

$$\eta_\gamma = \frac{\left(\frac{dC_{M_x}}{dx_{\gamma_i}}\right)_e}{\left(\frac{dC_{M_x}}{dx_{\gamma_i}}\right)_r}, \tag{12}$$

where dC_{M_x}/dx_{γ_i} is the derivative of total root bending moment of the aircraft with respect to each twist variable. The “e” subscript denotes the elastic or aerostructural derivative, while the the “r” subscript denotes the rigid or aerodynamic derivative. The elastic derivative can be computed by

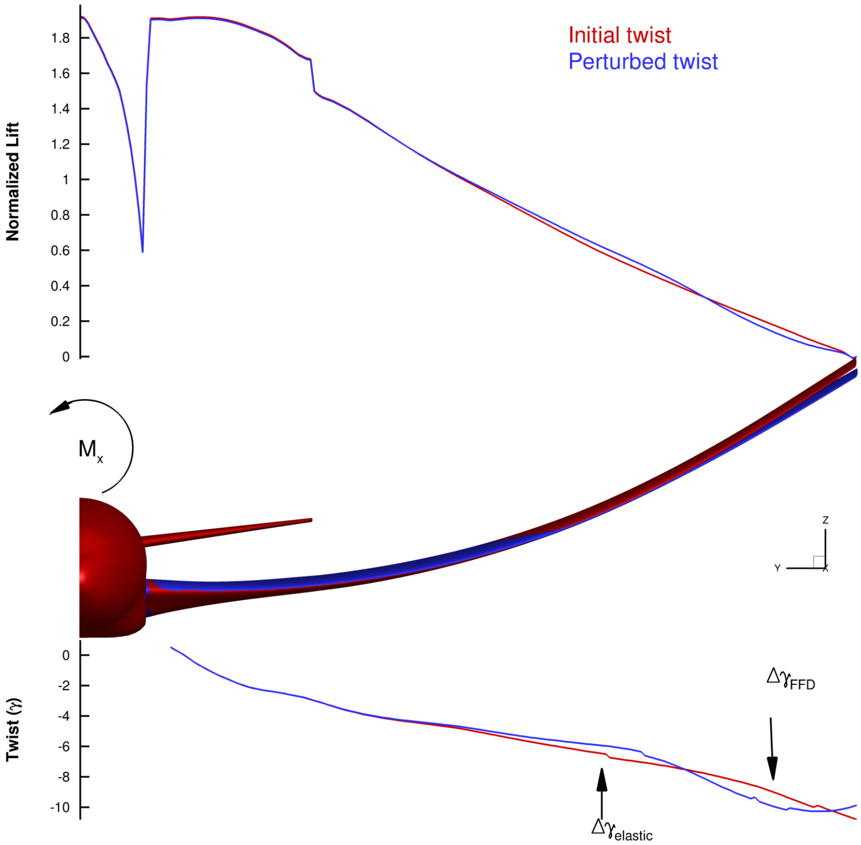

Figure 15: Example of loss in FFD twist sensitivity of bending moment due to aeroelastic deformation.

solving the coupled adjoint for the aerostructural problem. The rigid derivative can be computed by freezing the aeroelastic shape and solving only with the aerodynamic adjoint. This value provides a measurement of how much sensitivity is lost for each spanwise twist variable due to aeroelastic effects. When the aeroelastic effects are small, this value should be close to unity.

The twist effectiveness for the 2.5 g maneuver condition of the fixed-ply-orientation conventional and tow-steered optimized designs on both the uCRM-9 and uCRM-13.5 are compared in Figure 16. As expected, this value is closer to unity near the root of the wing, where the aeroelastic effects are smallest. As we move along the wing span toward the tip, the effectiveness declines. For the most flexible cases, this value actually becomes slightly negative, meaning that when these sections are geometrically twisted up, the bending moment would actually decrease due to the effect of the aeroelastic deflections inboard, a phenomenon similar to control reversal.

The loss of control effectiveness is an aeroelastic phenomenon typically seen in very flexible aircraft wings. This trend is typically exacerbated as the bend-twist coupling in the wing is increased, often by sweeping the wing further back. From Figure 16, we can see that for the uCRM-9 cases, as the optimizer increases the bend-twist coupling of the tow-steered design, the

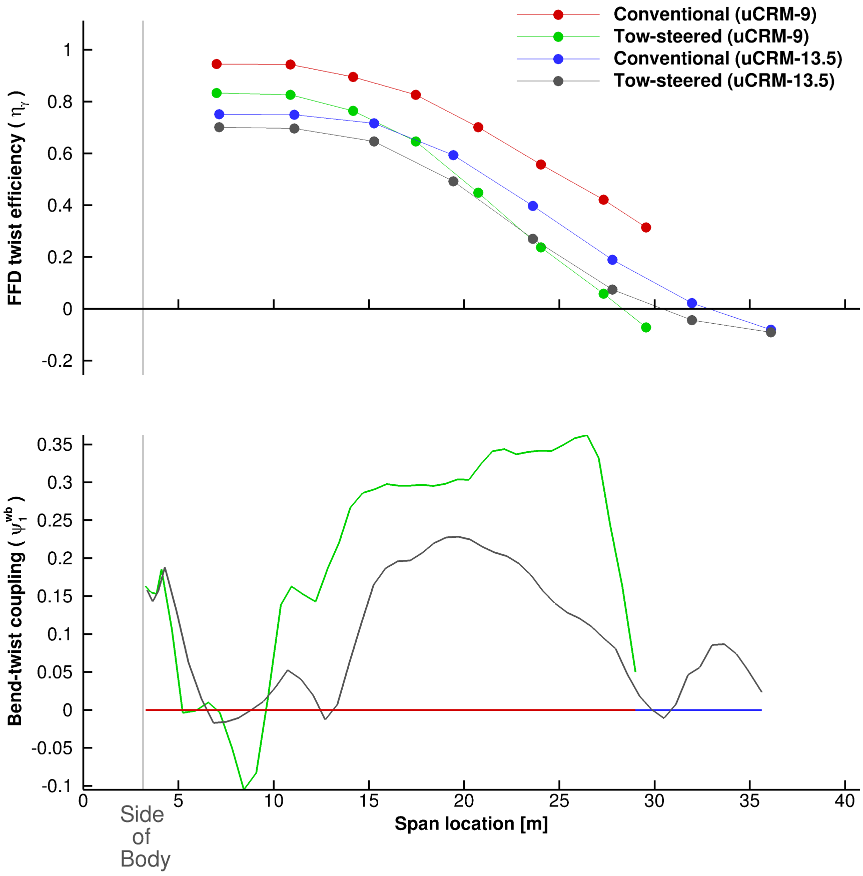

Figure 16: Comparison of twist effectiveness for root bending moment 2.5 g maneuver.

bending moment becomes less sensitive to the wing twist, especially near the tips, where the optimizer increases the coupling the most. This decrease in sensitivity at the tips may prevent the optimizer from utilizing even more coupling, ultimately limiting the amount of load alleviation that is possible. It can also be seen that the uCRM-13.5 designs have a lower effectiveness than the uCRM-9 designs, due to the increase in wing flexibility. Because the unsteered uCRM-13.5 design already starts with low sensitivity near the tip of the wing, the optimizer is not able to add any further coupling in this region on the tow-steered design, preventing further load alleviation benefits.

A previously mentioned, a third scale wingbox based on our uCRM-13.5 with optimized tow-steered composites was built by Aurora Flight Sciences. The wingbox was then tested at NASA Armstrong Research Center. The tests consisted of ground vibration testing and static loading. Figure 17 shows a photo of the tape being laid down by the AFP machine in the manufacturing of the optimized tow-steering wingbox and a photo of the static test for the same wingbox.

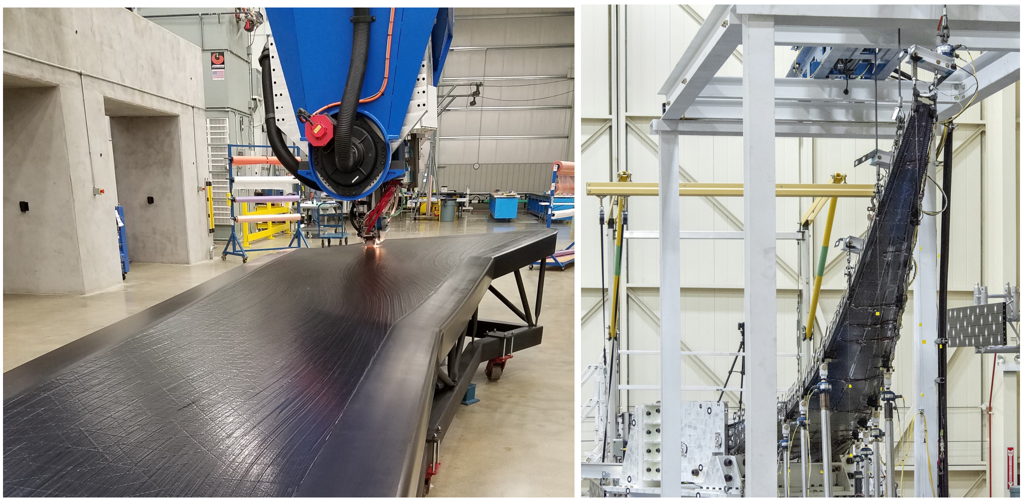

Figure 17: AFP machine manufacturing the tow-steered optimized uCRM-13.5 wingbox (left; courtesy of Aurora Flight Sciences). Static test of the same wing (right; courtesy of NASA)

[3]

8.3. *Effect of Varying Aspect Ratio*

In the previous sections, we examined the aerostructural design benefits offered by adding tow steering to wings of aspect ratios 9 and 13.5. We now extend this study by performing a sweep of optimizations of tow-steered and conventional composite designs with varying wing aspect ratios. This is accomplished by taking the uCRM-9 design optimization problem and adding planform variables—span, sweep, and chord—to the FFD variables. The optimization for each design is then run with a series of different aspect ratio constraints (AR = [7.5, 9, 10.5, 12, 13.5]). The cases for AR = 9 are equivalent to the uCRM-9 tow-steered and conventional optimized cases presented earlier. The AR = 13.5 cases are not exactly the same as the uCRM-13.5 results presented earlier. The uCRM-9 and uCRM-13.5 designs feature different number of ribs, wing taper ratio, and fuselage positioning, none of which is varied during this aspect ratio study on the uCRM-9. Therefore, the resulting 13.5-aspect-ratio version of the uCRM-9 ends up being slightly different. The wing planform for each aspect ratio is shown in Figure 18.

The trend for fuel burn, MTOW, L/D, and wing structural mass for the optimal-fuel-burn designs as a function of aspect ratio is shown in Figure 19. Adding tow steering to the design decreases fuel burn, MTOW, and wing mass for all aspect ratio designs. Similarly to the previous cases, L/D is largely unaffected by the use of tow steering. As the aspect ratio increases, the fuel burn decreases. However, toward the higher-aspect-ratio end, the benefit in fuel burn begins to decrease. By analyzing the trend in L/D, we deduce that this is because as the aspect ratio increases, the amount of induced drag on the design left to be reduced becomes smaller, while the viscous and compressibility drag begin to dominate. Analyzing the trend in MTOW, we see that as the aspect ratio increases, the MTOW decreases, except for AR = 13.5. By comparing the

---

[3] `www.nasa.gov`

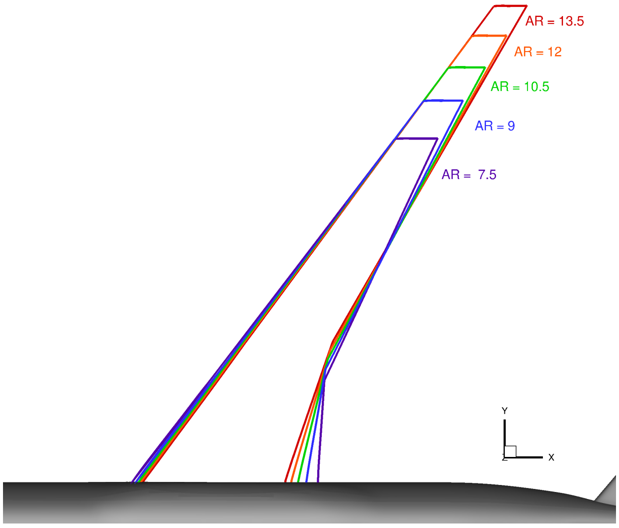

Figure 18: uCRM planforms for variable-aspect-ratio study

trends in fuel burn and wing mass, we find that this increase in MTOW is due to the fact that as the aspect ratio increases, the improvements in fuel burn begin to taper off, while the rate of increase in wing mass continues to increase. This causes the increase in wing structural mass to eventually outpace the decrease in fuel burn, which leads to an increase in MTOW.

The trend for passive load alleviation of each design can be seen in Figure 20. All designs tend towards an elliptical lift distribution at cruise with some load alleviation at the 2.5 g maneuver condition. The tow-steered AR = 7.5 case exhibits a prominent dip in the 2.5 g lift distribution, indicating flow separation. This indicates that lower-aspect-ratio designs are more susceptible to this type of flow separation. The reason for this is likely because, according to Figure 19, these designs have higher maximum takeoff weights, meaning that the designs have to meet higher lift requirements for their maneuver conditions. We also see that as the aspect ratio increases, the amount of bend-twist coupling utilized on the tow-steered design by the optimizer, particularly near the tip, decreases. This confirms the trend seen earlier in Section 8.2: As the aspect ratio of the wing increases, the amount of additional load alleviation used by the tow-steered design decreases.

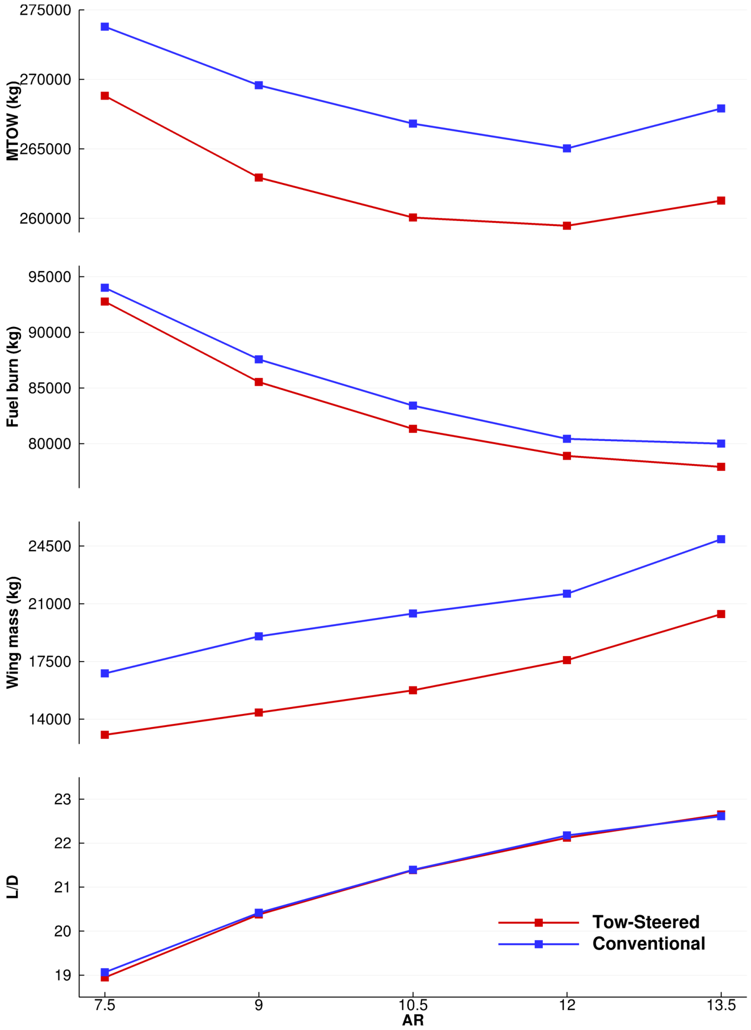

Figure 19: Fuel burn, MTOW, L/D, and wing mass trends for increasing aspect ratio

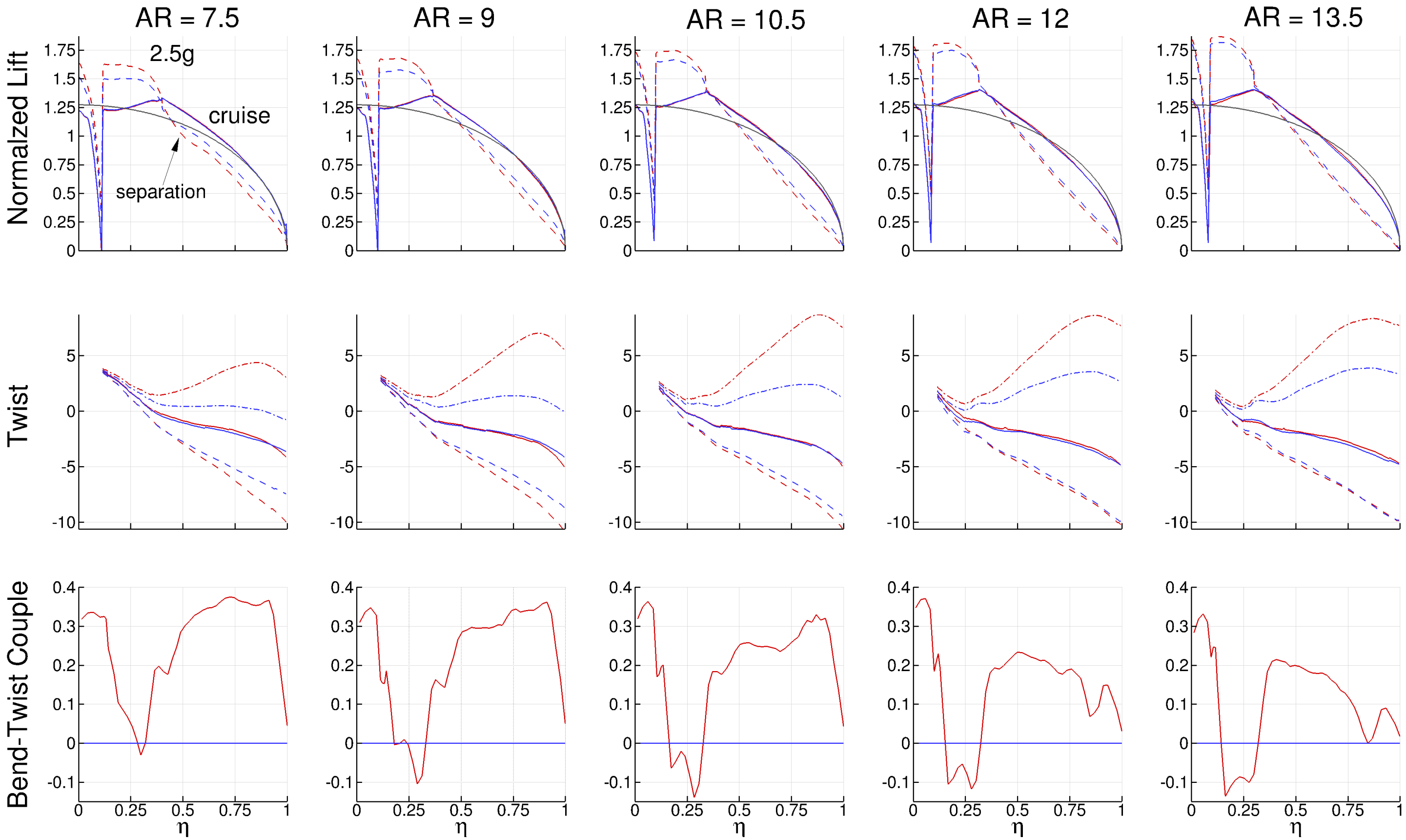

Figure 20: Passive load alleviation trend for increasing aspect ratio; tow-steered design (red), conventional design (blue).

9. Conclusions

In this series of design optimization studies, we investigated the aeroelastic benefits of tow steering as applied to flexible-wing design. To accomplish this, we performed a series of high-fidelity, gradient-based aerostructural fuel burn optimizations using both tow-steered and conventional composite wing designs for the uCRM-9 and uCRM-13.5 designs. The aerodynamics were modeled with a RANS-based CFD solver, and wing structure was modeled with a 3D CSM solver using shell finite elements. The optimization problem included both geometric variables (airfoil shapes and twist) and structural sizing variables (component thicknesses and tow path). Comparing the results of each design optimization provided insights into the benefits that tow-steering manufacturing has to offer for flexible-wing design.

The first set of insights came from the results run on the uCRM-9 model, which is representative of a Boeing-777-type aircraft. These results are summarized in Table 9. From these results, we found that the aircraft fuel burn and MTOW could be reduced by 2.3% and 2.5%, respectively, relative to a conventional composite design. This improvement is due to a 24% reduction in structural weight of the tow-steered design, owed to improvements in the design's structural and aeroelastic tailoring. When the conventional composite design is allowed to rotate the plies in the skins, the improvements in fuel burn and MTOW offered by tow steering was reduced to 1.4% and 1.5%, respectively, while the structural weight reduction was 15.7%. This is because the optimizer is largely able to match the load alleviation performance of the tow-steered design with the conventional design. We determined that 0.9% of the 2.3% decrease in fuel burn seen in the comparison between the tow-steered and conventional design's performance was due to the additional load alleviation, while the remaining amount came from structural tailoring.

Table 9: Summary of results for uCRM-9 aerostructural optimization studies using tow-steered composite (TS), fixed-ply-orientation conventional composite (C), and conventional rotated-ply-orientation composite (CR).

Quantity	TS	C	CR
Fuel Burn [kg]	85 535	87 558	86 745
MTOW [kg]	262 937	269 575	266 831
Wing mass [kg]	14 402	19 016	17 086

For the uCRM-13.5 optimization studies, we found that the tow-steered wing reduced the structural weight of the wingbox by 14% and the fuel burn by 1.5%. This was possible in large part by the increase in local structural tailoring of the wing design. When compared to the uCRM-9 design, the uCRM-13.5 tow-steered design featured nearly no passive load alleviation improvement relative to the conventional composite design. This suggests that aspect ratio plays a critical role in the amount of load alleviation that is possible for the tow-steered design.

To investigate the trend with aspect ratio, we ran optimizations with wing aspect ratios varying from 7.5 to 13.5. The trends indicate diminishing returns in fuel burn improvement for increasing wing aspect ratio. This is because the amount of additional load alleviation enabled by tow steering relative to the conventional design decreased with increasing aspect ratio.

The results presented here show that tow-steered wing designs have the potential to decrease aircraft fuel burn and structural weight relative to conventional composite designs. Further work using the presented methodology could provide additional insights. As mentioned previously, the laminate ply fractions used in this work were fixed throughout the optimization. However, additional improvements would likely be possible for both the conventional and tow-steered designs by allowing the optimizer to spatially vary the ply fraction distribution throughout the structure. Additionally, further buckling performance improvements could materialize by giving the optimizer control over the stacking sequence of the wingbox laminates.

A third scale model of our optimal 13.5-aspect-ratio, tow-steered wingbox was manufactured by Aurora Flight Sciences using their AFP machine. This wingbox was recently structurally tested by NASA, and the preliminary results were in good agreement with model predictions [4].

Further insight might be revealed by allowing the optimizer to vary the wing planform—sweep, span, and chord. This would allow the optimizer to find the optimal wing aspect ratio and planform to minimize fuel burn for both a tow-steered and conventional composite design. It would also be worth quantifying the effect that changing the optimization objective would have on both the tow-steered and conventional composite wing designs. This could be accomplished by producing a Pareto front between two objectives: one that focuses more on structural performance (e.g., structural weight or TOGW) and another that focuses on aerodynamics (e.g., fuel burn or drag).

Finally, we only considered three flight conditions—a cruise condition, a 2.5 g pull-up maneuver, and a -1 g push-over maneuver. This was done to simplify the problem and make it easier to interpret the results from the aerostructural optimizations. Previous work on high-fidelity aerostructural design optimization has shown the need for considering multiple cruise flight conditions and constraints, such as gust loading, flutter [15, 16, 47], and buffet onset [46] to achieve more realistic designs. Flutter in particular would likely be an active sizing constraint for the higher-aspect-ratio wing designs presented in this work. Nevertheless, the work presented herein provides new insights into the design of tow-steered composite wings, and provides a framework for other multidisciplinary design optimization studies of tow-steered composite structures.

Acknowledgements

This work was partially supported by NASA through award number NNL15AA01C (Advanced Air Transport Technology project, technical lead Karen Taminger). The computational results in this work were enabled by the Extreme Science and Discovery Environment (XSEDE) funded through the National Science Foundation (NSF) through grant number ACI-1053575. The authors would also like to acknowledge Benjamin Smith (Aurora Flight Sciences) for his insight into the manufacturing process for tow-steered laminates, and Carlos Cesnik (University of Michigan) for the various discussions.

References

[1] D. H.-J. A. Lukaszewicz, C. Ward, K. D. Potter, The engineering aspects of automated prepreg layup: History, present and future, Composites Part B: Engineering 43 (2012) 997–1009.

[2] J. Sloan, ATL and AFP: Defining the megatrends in composite aerostructures, https://www.compositesworld.com/articles/atl-and-afp-defining-the-megatrends-in-composite-aerostructures, 2008. URL: `https://www.compositesworld.com/articles/atl-and-afp-defining-the-megatrends-in-composite-aerostructures`, last accessed on Jan 20, 2019.

[3] C. Grant, Automated processes for composite aircraft structure, Industrial Robot 33 (2006) 117–121. doi:`10.1108/01439910610651428`.

---

[4] `https://www.nasa.gov/centers/armstrong/features/PAT_Experimental_Wing_Verified_During_Loads_Testing.html`, Last accessed on January 20, 2019.

[4] A. Khani, S. IJsselmuiden, M. Abdalla, Z. Gurdal, Design of variable stiffness panels for maximum strength using lamination parameters, Composites Part B: Engineering 42 (2011) 546–552.

[5] C. Lopes, Z. Gurdal, P. Camanho, Tailoring for strength of composite steered-fibre panels with cutouts, Composites Part A: Applied Science and Manufacturing 41 (2010) 1760–1767.

[6] M. W. Hyer, R. F. Charette, Use of curvilinear fiber format in composite structure design, AIAA Journal 29 (1991) 1011–1015. doi:10.2514/3.10697.

[7] S. T. Ijsselmuiden, M. M. Abdalla, Z. Gurdal, Optimization of variable-stiffness panels for maximum buckling load using lamination parameters, AIAA Journal 48 (2010) 134–143. doi:10.2514/1.42490.

[8] S. Setoodeh, M. M. Abdalla, S. T. IJsselmuiden, Z. Gurdal, Design of variable-stiffness composite panels for maximum buckling load, Composite Structures 87 (2009) 109–117.

[9] M. Hyer, H. Lee, The use of curvilinear fiber format to improve buckling resistance of composite plates with central circular holes, Composite Structures 18 (1991) 239–261.

[10] B. C. Kim, P. M. Weaver, K. Potter, Manufacturing characteristics of the continuous tow shearing method for manufacturing of variable angle tow composites, Composites Part A: Applied Science and Manufacturing 61 (2014) 141–151.

[11] B. F. Tatting, Z. Gurdal, Design and manufacture of elastically tailored tow placed plates, Technical Report NASA/CR-2002-211919, NASA, Langley Research Center, Hampton, VA, 2002.

[12] A. Haavajõe, M. Mikola, M. Pohlak, Design and Manufacturing of Variable Angle Tow Laminate, volume 674, 2016.

[13] G. Warwick, Aurora builds tow-steered carbon wing for NASA, Aviation Week & Space Technology 179 (2017).

[14] J. E. Hale, Boeing 787 from the ground up, Aero Magazine (2006).

[15] O. Stodieck, J. E. Cooper, P. M. Weaver, P. Kealy, Aeroelastic tailoring of a representative wing box using tow-steered composites, AIAA Journal 55 (2017) 1425–1439. doi:10.2514/1.j055364.

[16] B. K. Stanford, C. V. Jutte, Comparison of curvilinear stiffeners and tow steered composites for aeroelastic tailoring of aircraft wings, Computers & Structures 183 (2017) 48 – 60. doi:https://doi.org/10.1016/j.compstruc.2017.01.010.

[17] G. K. W. Kenway, G. J. Kennedy, J. R. R. A. Martins, Scalable parallel approach for high-fidelity steady-state aeroelastic analysis and derivative computations, AIAA Journal 52 (2014) 935–951. doi:10.2514/1.J052255.

[18] J. R. R. A. Martins, J. T. Hwang, Review and unification of methods for computing derivatives of multidisciplinary computational models, AIAA Journal 51 (2013) 2582–2599. doi:10.2514/1.J052184.

[19] G. K. W. Kenway, J. R. R. A. Martins, Multipoint high-fidelity aerostructural optimization of a transport aircraft configuration, Journal of Aircraft 51 (2014) 144–160. doi:10.2514/1.C032150.

[20] Z. Lyu, G. K. Kenway, C. Paige, J. R. R. A. Martins, Automatic differentiation adjoint of the Reynolds-averaged Navier–Stokes equations with a turbulence model, in: 21st AIAA Computational Fluid Dynamics Conference, San Diego, CA, 2013. doi:10.2514/6.2013-2581.

[21] G. K. W. Kenway, N. Secco, J. R. R. A. Martins, A. Mishra, K. Duraisamy, An efficient parallel overset method for aerodynamic shape optimization, in: Proceedings of the 58th AIAA/ASCE/AHS/ASC Structures, Structural Dynamics, and Materials Conference, AIAA SciTech Forum, Grapevine, TX, 2017. doi:10.2514/6.2017-0357.

[22] C. A. Mader, J. R. R. A. Martins, J. J. Alonso, E. van der Weide, ADjoint: An approach for the rapid development of discrete adjoint solvers, AIAA Journal 46 (2008) 863–873. doi:10.2514/1.29123.

[23] G. J. Kennedy, J. R. R. A. Martins, A parallel finite-element framework for large-scale gradient-based design optimization of high-performance structures, Finite Elements in Analysis and Design 87 (2014) 56–73. doi:10.1016/j.finel.2014.04.011.

[24] L. Uyttersprot, Inverse Distance Weighting Mesh Deformation, Ph.D. thesis, Delft University of Technology, 2014.

[25] S. A. Brown, Displacement extrapolation for CFD+CSM aeroelastic analysis, in: Proceedings of the 35th AIAA Aerospace Sciences Meeting, Reno, NV, 1997. AIAA 1997-1090.

[26] J. R. R. A. Martins, J. J. Alonso, J. J. Reuther, A coupled-adjoint sensitivity analysis method for high-fidelity aerostructural design, Optimization and Engineering 6 (2005) 33–62. doi:10.1023/B:OPTE.0000048536.47956.62.

[27] P. E. Gill, W. Murray, M. A. Saunders, An SQP algorithm for large-scale constrained optimization, Society for Industrial and Applied Mathematics 47 (2005).

[28] R. E. Perez, P. W. Jansen, J. R. R. A. Martins, pyOpt: A Python-based object-oriented framework for nonlinear constrained optimization, Structural and Multidisciplinary Optimization 45 (2012) 101–118. doi:10.1007/s00158-011-0666-3.

[29] J. C. Vassberg, M. A. DeHaan, S. M. Rivers, R. A. Wahls, Development of a common research model for applied CFD validation studies, 2008. AIAA 2008-6919.

[30] T. R. Brooks, G. K. W. Kenway, J. R. R. A. Martins, Benchmark aerostructural models for the study of transonic aircraft wings, AIAA Journal 56 (2018) 2840–2855. doi:10.2514/1.J056603.

[31] G. J. Kennedy, J. R. R. A. Martins, A parallel aerostructural optimization framework for aircraft design studies, Structural and Multidisciplinary Optimization 50 (2014) 1079–1101. doi:10.1007/s00158-014-1108-9.

[32] M. L. Bucalem, K.-J. Bathe, Higher-order MITC general shell elements, International Journal for Numerical Methods in Engineering 36 (1993) 3729–3754. doi:`10.1002/nme.1620362109`.

[33] T. R. Brooks, G. J. Kennedy, J. R. R. A. Martins, High-fidelity aerostructural optimization of a high aspect ratio tow-steered wing, in: 57th AIAA/ASCE/AHS/ASC Structures, Structural Dynamics, and Materials Conference, American Institute of Aeronautics and Astronautics, 2016. doi:`10.2514/6.2016-1179`.

[34] T. R. Brooks, G. J. Kennedy, J. R. R. A. Martins, High-fidelity multipoint aerostructural optimization of a high aspect ratio tow-steered composite wing, in: Proceedings of the 58th AIAA/ASCE/AHS/ASC Structures, Structural Dynamics, and Materials Conference, AIAA SciTech Forum, Grapevine, TX, 2017. doi:`10.2514/6.2017-1350`.

[35] D. Liu, V. Toropov, D. Barton, O. Querin, Two methodologies for stacking sequence optimization of laminated composite materials, in: Computational Structural Engineering, Springer Netherlands, Dordrecht, 2009, pp. 909–915.

[36] G. Kreisselmeier, R. Steinhauser, Application of vector performance optimization to a robust control loop design for a fighter aircraft, International Journal of Control 37 (1983) 251–284.

[37] A. B. Lambe, J. R. R. A. Martins, G. J. Kennedy, An evaluation of constraint aggregation strategies for wing box mass minimization, Structural and Multidisciplinary Optimization 55 (2017) 257–277. doi:`10.1007/s00158-016-1495-1`.

[38] W. J. Stroud, N. Agranoff, Minimum-mass design of filamentary composite panels under combined loads: Design procedure based on simplified buckling equations, Technical Report TN-D-8257, NASA Langley Research Center, Hampton, VA, 1976.

[39] G. J. Kennedy, G. K. W. Kenway, J. R. R. A. Martins, High aspect ratio wing design: Optimal aerostructural tradeoffs for the next generation of materials, in: Proceedings of the AIAA Science and Technology Forum and Exposition (SciTech), National Harbor, MD, 2014. AIAA-2014-0596.

[40] G. J. Kennedy, G. K. Kenway, J. R. R. A. Martins, A Comparison of Metallic, Composite and Nanocomposite Optimal Transonic Transport Wings, Technical Report, NASA, 2014. CR-2014-218185.

[41] T. R. Brooks, J. R. R. A. Martins, On manufacturing constraints for tow-steered composite design optimization, Composite Structures 204 (2018) 548–559. doi:`10.1016/j.compstruct.2018.07.100`.

[42] M. H. Shirk, T. J. Hertz, T. A. Weisshaar, Aeroelastic tailoring — theory, practice, and promise, Journal of Aircraft 23 (1986) 6–18. doi:`10.2514/3.45260`.

[43] T. W. Sederberg, S. R. Parry, Free-form deformation of solid geometric models, SIGGRAPH Comput. Graph. 20 (1986) 151–160. doi:`10.1145/15886.15903`.

[44] G. K. Kenway, G. J. Kennedy, J. R. R. A. Martins, A CAD-free approach to high-fidelity aerostructural optimization, in: Proceedings of the 13th AIAA/ISSMO Multidisciplinary Analysis Optimization Conference, AIAA 2010-9231, Fort Worth, TX, 2010. doi:`10.2514/6.2010-9231`.

[45] Federal Aviation Administration, Federal aviation regulations, part 25 — airworthiness standards: Transport category airplanes, 2009. URL: `http://www.faa.gov/regulations_policies/`.

[46] G. K. W. Kenway, J. R. R. A. Martins, Buffet onset constraint formulation for aerodynamic shape optimization, AIAA Journal 55 (2017) 1930–1947. doi:`10.2514/1.J055172`.

[47] E. Jonsson, C. A. Mader, G. J. Kennedy, J. R. R. A. Martins, Computational modeling of flutter constraint for high-fidelity aerostructural optimization, in: 2019 AIAA/ASCE/AHS/ASC Structures, Structural Dynamics, and Materials Conference, American Institute of Aeronautics and Astronautics, San Diego, CA, 2019. doi:`10.2514/6.2019-2354`.